Lithos 308–309 (2018) 65–82

Contents lists available at ScienceDirect

Lithos

journal homepage: www.elsevier.com/locate/lithos

# The origin of secondary heavy rare earth element enrichment in carbonatites: Constraints from the evolution of the Huanglongpu district, China

M. Smith [a,*], J. Kynicky [b], Chen Xu [c], Wenlei Song [c], J. Spratt [d], T. Jeffries [d], M. Brtnicky [b], A. Kopriva [b,e], D. Cangelosi [f]

[a] School of Environment and Technology, University of Brighton, Brighton, UK
[b] Mendel University in Brno, Zemedelska 1, CZ-613 00 Brno, Czech Republic
[c] Peking University, School of Earth & Space Science, Laboratory for Orogenic Belts & Crustal Evolution, Beijing 100871, PR China
[d] Department of Earth Sciences, The Natural History Museum, London, UK
[e] TESCAN Brno, s.r.o., Libusina 1, CZ-623 00 Brno, Czech Republic
[f] School of Earth and Environment, University of Leeds, Leeds LS2 9JT, UK

ARTICLE INFO

*Article history:*
Received 27 October 2017
Accepted 25 February 2018
Available online 04 March 2018

*Keywords:*
Rare earth elements
Carbonatite
Hydrothermal
Sulphate
Brine

ABSTRACT

The silico-carbonatite dykes of the Huanglongpu area, Lesser Qinling, China, are unusual in that they are quartz-bearing, Mo-mineralised and enriched in the heavy rare earth elements (HREE) relative to typical carbonatites. The textures of REE minerals indicate crystallisation of monazite-(Ce), bastnäsite-(Ce), parisite-(Ce) and aeschynite-(Ce) as magmatic phases. Burbankite was also potentially an early crystallising phase. Monazite-(Ce) was subsequently altered to produce a second generation of apatite, which was in turn replaced and overgrown by britholite-(Ce), accompanied by the formation of allanite-(Ce). Bastnäsite and parisite where replaced by synchysite-(Ce) and röntgenite-(Ce). Aeschynite-(Ce) was altered to uranopyrochlore and then pyrochlore with uraninite inclusions. The mineralogical evolution reflects the evolution from magmatic carbonatite, to more silica-rich conditions during early hydrothermal processes, to fully hydrothermal conditions accompanied by the formation of sulphate minerals. Each alteration stage resulted in the preferential leaching of the LREE and enrichment in the HREE. Mass balance considerations indicate hydrothermal fluids must have contributed HREE to the mineralisation. The evolution of the fluorcarbonate mineral assemblage requires an increase in $a_{Ca^{2+}}$ and $a_{CO_3^{2-}}$ in the metasomatic fluid (where $a$ is activity), and breakdown of HREE-enriched calcite may have been the HREE source. Leaching in the presence of strong, LREE-selective ligands ($Cl^-$) may account for the depletion in late stage minerals in the LREE, but cannot account for subsequent preferential HREE addition. Fluid inclusion data indicate the presence of sulphate-rich brines during alteration, and hence sulphate complexation may have been important for preferential HREE transport. Alongside HREE-enriched magmatic sources, and enrichment during magmatic processes, late stage alteration with non-LREE-selective ligands may be critical in forming HREE-enriched carbonatites.



## 1. Introduction

The rare earth elements (REE) (here defined as the lanthanides plus Y), have long been a focus of research because of their utility as tracers for geochemical processes from magma source and differentiation, through to hydrothermal system evolution (e.g. Chakhmouradian, 2006; Haas et al., 1995; Henderson, 1984; Migdisov et al., 2009). In recent years they have also become a focus of intense economic interest because of the restriction in supply caused by a focus of production in China, coupled with increasing use in renewable energy and high technology applications (Chakhmouradian and Wall, 2012). Rare earth element resources are dominated by concentrations, either from magmatic or hydrothermal processes, associated with alkaline igneous rocks, notably carbonatites. A significant issue with primary resources is that carbonatite concentrations tend to be preferentially enriched in the light REE (La to Nd), which, with the exception of Nd, are less economically important than the heavy REE (Eu to Lu) (Chakhmouradian and Wall, 2012). Middle to HREE enriched carbonatites do occur however, and are of great interest both because of their economic potential, and because of the need to understand the processes leading to this enrichment (e.g. Xu et al., 2007). Hydrothermal processes have been shown to fractionate the REE via differential solubility during leaching of primary phases, controls on relative solubility exerted by

* Corresponding author.
*E-mail address:* martin.smith@brighton.ac.uk (M. Smith).

https://doi.org/10.1016/j.lithos.2018.02.027
0024-4937/

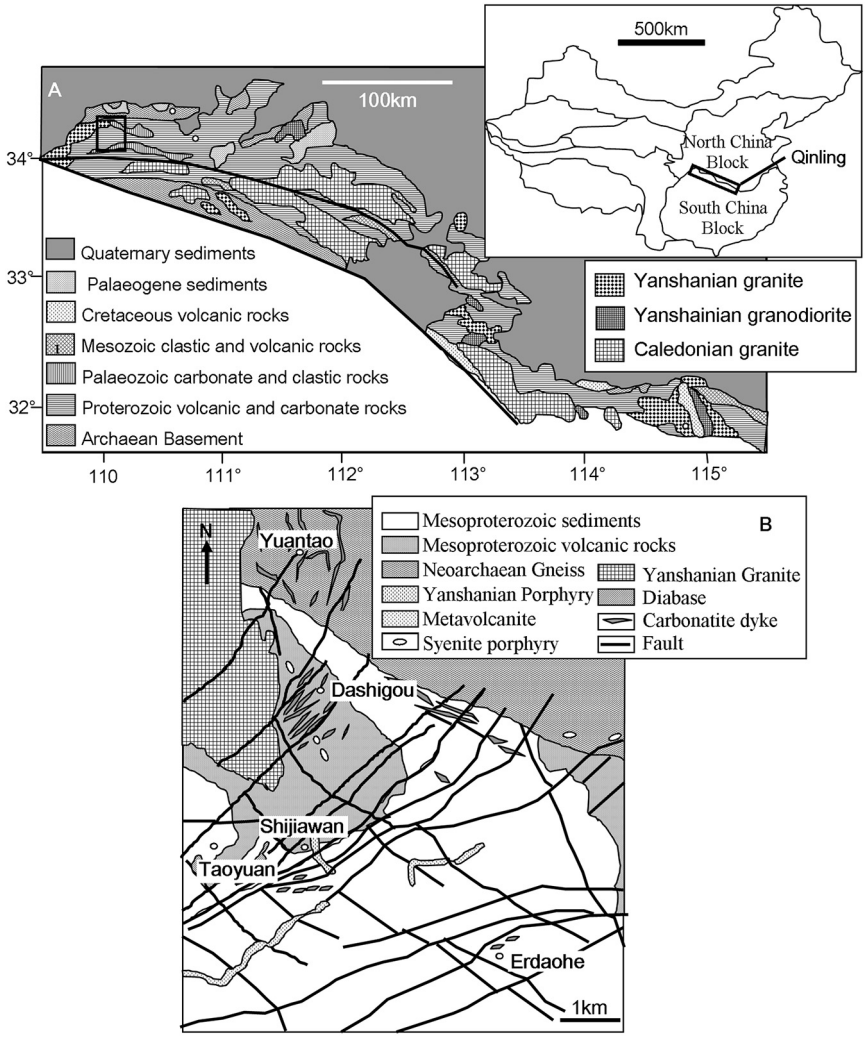


**Fig. 1.** (A) Geological map of the eastern Qinling mountains showing the location of the Huanglongpu area. Inset shows the overall location within China in relation to major crustal blocks. (B) Geological map of the Huanglongpu Mo-district (highlighted in bold in A). Maps adapted from Xu et al. (2010). Samples labelled HLP are from the Dashigou site, samples labelled YT are from Yuantao.

the variation in the stability of aqueous complex ions with different ligands (Haas et al., 1995; Migdisov et al., 2009; Wood, 1990), variation in the relative solubility of secondary phases, and all of these coupled with dynamic flow and reaction pathways (Williams-Jones et al., 2013). In this study we have investigated the paragenetic and chemical evolution of rare earth minerals in the Huanglongpu carbonatites, Qinling Mountains, China (Fig. 1; Xu et al., 2007, 2010; Song et al., 2015). These carbonatites are exceptional because of their association with economic molybdenite mineralisation, a relatively silica-rich geochemistry and hence an association with quartz, and a relative enrichment in the HREE compared to typical carbonatites (Kynicky et al., 2012). The exceptional geochemistry of the dykes, and the preservation of a wide range of reaction textures, make this an ideal site to assess the role of post-magmatic processes in the genesis of HREE-enriched carbonatites globally. Heavy rare earth enrichment has been reported from a number of carbonatites, typically associated with late stage hydrothermal phenomena (e.g. Tundulu - Ngwenya, 1993; Songwe - Swinden and Hall, 2012; Bear Mountain - Moore et al., 2017; Lofdal - Bodeving et al., 2017). Bulk rock analyses of the Huanglongpu carbonatites show that their REE patterns are transitional between more typical carbonatites and the HREE-enriched hydrothermal deposits (Fig. 2). Thus the Huanglongpu district may provide an exceptionally well exposed site, suitable for characterisation of hydrothermal enrichment process, with wider implications for HREE-enrichment in carbonatites globally.

## 2. Geological setting

The Huanglongpu district is composed of four carbonatite-related orefields with a total ore reserve of >180 Kt of Mo. Almost all spatially

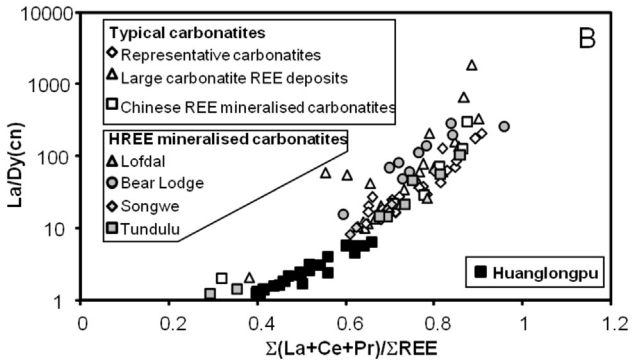


**Fig. 2.** Comparison of ratios characterising the REE pattern for the Huanglongpu carbonatites with Chinese REE mineralised carbonatites (Kynicky et al., 2012), typical carbonatites (Hornig-Kjarsgaard, 1998), and carbonatites with reported high HREE contents (Bodeving et al., 2017; Moore et al., 2017; Ngwenya, 1993; Swinden and Hall, 2012) Data from Huanglongpu from Xu et al. (2010), Kynicky et al. (2012) and Song et al. (2015). Chondrite values from Sun and McDonough (1989) here and throughout.

**Table 1**
Localities and descriptions of samples used in this study.

| | Locality* | | Deposit | Sample description | Analysed REE and associated minerals# |
|---|---|---|---|---|---|
| | Longitude | Latitude | | | |
| HLP1 | 410,530 | 3,803,439 | Dashigou | Sulphide mineralised calcite-quartz carbonatite. | Mnz, Bst, Par, All |
| HLP2 | 410,530 | 3,803,439 | Dashigou | Sulphide mineralised calcite-quartz carbonatite. | Mnz, Ap, Brh, All, Par, Syn |
| HLP3 | 410,530 | 3,803,439 | Dashigou | Sulphide mineralised calcite-quartz carbonatite. | NA |
| HLP4 | 410,530 | 3,803,439 | Dashigou | Sulphide mineralised calcite-quartz carbonatite. | NA |
| HLP5 | 410,530 | 3,803,439 | Dashigou | Sulphide mineralised carbonatite. | Par, Syn, Rnt, Xen |
| HLP6 | 410,530 | 3,803,439 | Dashigou | Barite altered calcite carbonatite. | Mnz, Bst, Par, Xen |
| HLP7 | 410,530 | 3,803,439 | Dashigou | Sulphide mineralised calcite-quartz carbonatite. | Mnz |
| HLP10 | 410,530 | 3,803,439 | Dashigou | Sulphide-calcite veinlet cutting calcite-quartz carbonatite. | Mnz, Ap, Brh, All, Par, Syn |
| HLP15 | 410,530 | 3,803,439 | Dashigou | Sulphide mineralised calcite-quartz carbonatite. | Mnz, Pyc, Aesch, Par, Syn, Rnt |
| HLP A | 409,886 | 3,804,124 | Dashigou | Calcite-quartz carbonatite. | Ap |
| HLP B | 409,886 | 3,804,124 | Dashigou | Molybdenite mineralised calcite-quartz carbonatite. | Mnz |
| HLP C | 409,886 | 3,804,124 | Dashigou | Contact zone between calcite carbonatite and quartz-core. | Mnz |
| YT1 | 410,732 | 3,806,281 | Yuantao | Calcite-quartz carbonatite with minor sulphide veining. | Mnz |
| YT2 | 410,732 | 3,806,281 | Yuantao | Sulphate (barite-celestine) rich carbonatite. | Pyc, Aesch, Mnz, Bst, Par, Syn, Rnt |
| YT6 | 410,732 | 3,806,281 | Yuantao | Calcite-quartz carbonatite with minor sulphide veining. | Par, Syn, Rnt, Xen |

#Mineral abbreviations – Mnz –Monazite; Bst – Bastnäsite; Par – Parisite; Syn – Synchysite; Rnt – Röntgenite; All – Allanite; Brh – Britholite; Xen – Xenotime; Ap – apatite; Pyc – Pyrochlore; Aesch – Aeschynite.
* Grid reference format WGS84 sector 49S.

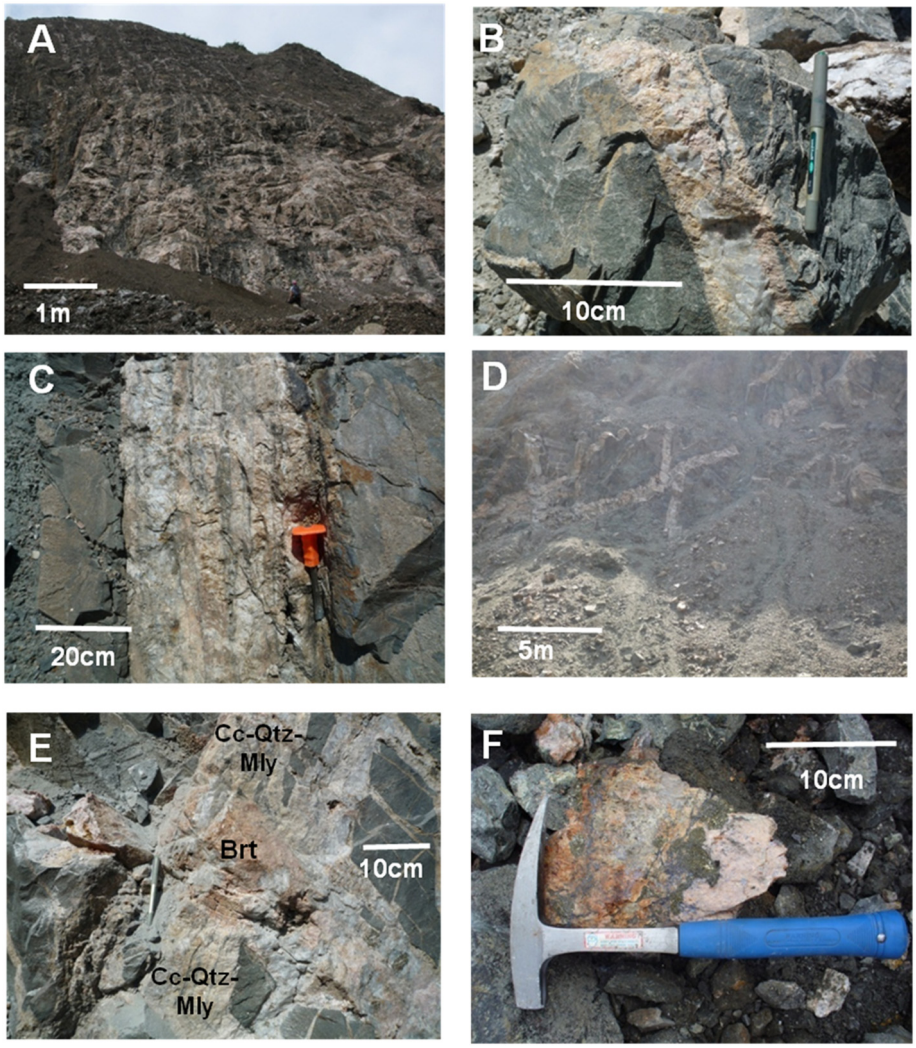


**Fig. 3.** Field relationships from Dashigou open pit. (A) Highly parallel carbonatite dykes and veins. Field of view ~ 30 m. Dykes are upto 3 m diameter, with narrowest examples 2–3 cm. (B) Internal structure of a single dyke with carbonate concentrated on the margins and quartz in the centre. Sulphide mineralisation concentrated at the margin between quartz and carbonate. Margins are fenitised. (C) Composite dyke showing multiple opening stages. (D) Intersecting dykes in conjugate orientation, but with offset of one dyke by the other. (E) Intersection of carbonate-quartz-molybdenite dyke with cross cutting barite-calcite vein/dyke. (F) Individual dyke section showing transition from carbonate-rich margins associated with K-feldspar, through a sulphide (pyrite-molybdenite-galena) zone to a central quartz-rich zone. Cc – calcite; Qtz – quartz; Mly – molybdenite; Brt – barite.

associated porphyry and porphyry-skarn Mo deposits in the Qinling belt formed in the Late Jurassic-Early Cretaceous, as indicated by molybdenite *Re*-Os dates ranging from 148 to 112 Ma (Huang et al., 1994; Mao et al., 2008), whereas molybdenite from the Huanglongpu deposits is much older, yielding Re-Os ages from 209 to 221 Ma and monazite U-Pb and Th-Pb ages from 208.9 ± 4.6 Ma and 213.6 ± 4.0 Ma (Huang et al., 1994; Song et al., 2016; Stein et al., 1997). Alkali granites and syenites have been identified in the area, but these are peraluminous, inferred to be derived from similar sources to the Mo-bearing granitoids (typically granodiorite) and have zircon U-Pb ages of 131 ± 1 Ma (Zhao et al., 2010), and are therefore unrelated to the carbonatites and REE-mineralisation. All these data indicate that the mineralisation of the dykes is not a result of overprint by subsequent magmatism.

The Huanglongpu deposits belong spatially and genetically to the Qinling orogenic belt which is subdivided into two main parts, North Qinling and South Qinling, separated by the Shangdan suture (Fig. 1). The northern border of the North Qinling is marked by a relatively narrow, straight, steep north-dipping fault zone, the Machaoying fault zone, which is strongly temporally and spatially associated with the Cenozoic rift basin in the north. The southern border of the South Qinling is separated from the South China block by the Mianlue suture. The detailed geological framework and tectonic evolution of the Qinling region have been described by Xue et al. (1996), Meng and Zhang (2000), and Ratschbacher et al. (2003), and also in the context of carbonatite evolution by Xu et al. (2010, 2014) and Song et al. (2015).

The ore bodies occur discontinuously over a total distance of 6 km and an area of 23 km$^2$. The distribution of carbonatites is predominantly controlled by a northwest-striking, extensional fault zone. The Huanglongpu Mo deposits consist of separate mineralised bodies at Yuantou, Wengongling, Dashigou, Shijiawan I, II, Taoyuan and Erdaohe (Fig. 1b). With the exception of Shijiawan I, which is hosted by granite porphyry, the rest of the deposits are associated with carbonatite dykes (Xu et al., 2007, 2010). The samples studied here come from the Yuantao (YT) and Dashigou (HLP) deposits (Table 1).

The carbonatite dykes are highly parallel, predominantly dipping N to NNW, at steep angles (strike/dip ~260/50–88°N) and consist of calcite, kutnahorite, quartz, potassium feldspar, barite, pyrite, galena, sphalerite, molybdenite, monazite, Ca-REE-fluorcarbonates, apatite, britholite, pyrochlore, uraninite, REE fluorides, burbankite, celestine, strontianite and brannerite. Minor fluorite is found at Shijiawan and Yuantao. The dykes range in thickness from ~10 m to ~0.1 m (Fig. 3A-C) with lateral extents ranging from 10 m to >1 km. Rarer dykes occur in orientations conjugate to the main set (strike/dip ~350/50–80°E; Fig. 3D). Minor offsets suggest this set may be slightly later than the main set, although the conjugate orientation and presence of conjugate veins merging with the main set (Fig. 3E) suggest they were very nearly contemporaneous. Where cross-cutting relationships can be clearly observed, barite-celestine bearing dykes and veins cut the earlier carbonate-quartz-sulphide bearing dykes (Fig. 3E). Alteration envelopes consisting of biotite, epidote, pyrite and anhydrite are developed at the selvages of the dykes (Fig. 3B). The carbonatite dykes are dominated by calcite and other carbonates along dyke margins, with central infills of quartz. Quartz is dominantly restricted to cores of dykes and may be mainly hydrothermal in origin (Fig. 3B), although some dykes are composite and the result of repeated opening events (Fig. 3C). This suggests the primary dykes may have been calico-carbonatite in composition although the bulk dyke composition is silico-carbonatite. In the carbonatites, molybdenite occurs mainly as disseminated grains and intergranular and fracture-hosted films (Fig. 3F), sometimes associated with pyrite, galena and sphalerite suggesting a subsolidus, hydrothermal origin for at least some of the sulphide assemblage. Disseminated molybdenite is also found along fractures in fenitized gneiss near its contact with the dykes.

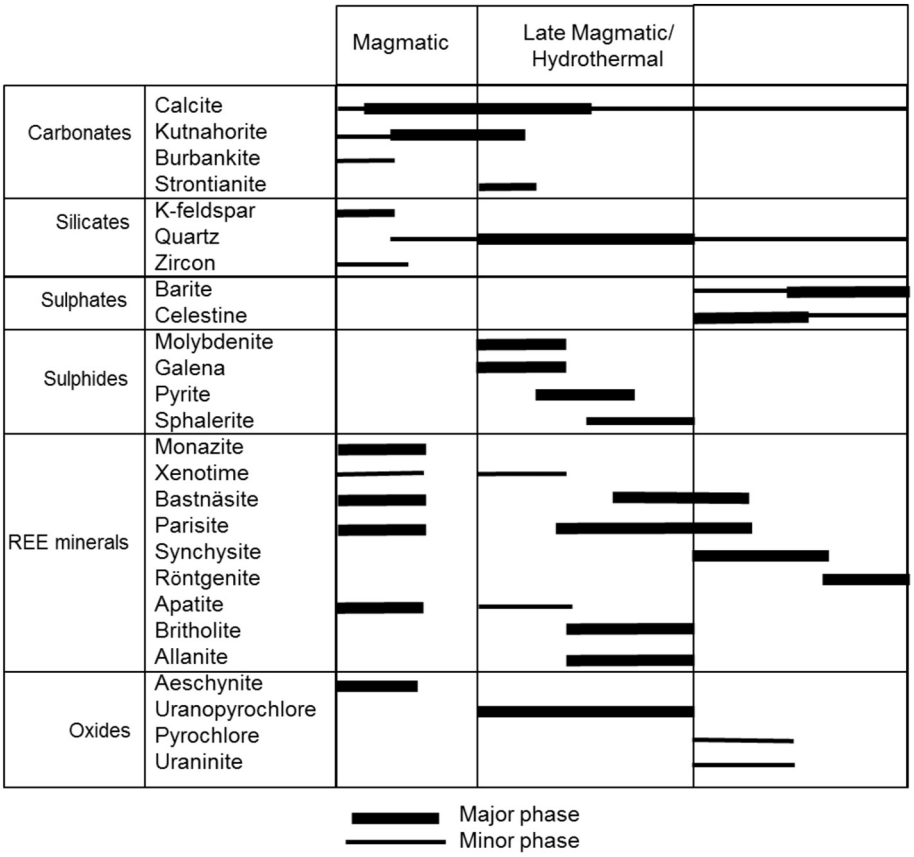


**Fig. 4.** Generalised summary of the major mineral paragenesis in the Huanglongpu deposits based on this study and observations in Xu et al. (2010, 2014), and Song et al. (2015).

## 3. Methods

### 3.1. Scanning electron microscopy

Scanning electron microscopic (SEM) observation of samples was carried out at Mendel University, Brno, Czech Republic, and the University of Brighton, UK. In Brno a FEG-SEM TESCAN MIRA 3 XMU was used. X-ray spectra were collected using either a Bruker Quantax 800 or Oxford Instruments XMax 80 EDX spectrometer using an accelerating voltage of 25 kV and a beam current of 5 nA. At Brighton a Zeiss EVO LS 15 SEM equipped with an Oxford Instruments XMax 80 EDX spectrometer was used, at 20 kV accelerating voltage and 1.2 nA beam current.

### 3.2. Electron microprobe

The major-element compositions of selected major and accessory mineral phases from the Huanglongpu carbonatites were measured by wavelength-dispersive X-ray spectrometry (WDS) using Cameca SX100 electron microprobes at the Joint Electron Microscopy and Microanalysis Laboratory, Institute of Geological Sciences, Masaryk University and Czech Geological Survey, and the Natural History Museum (NHM), London. At Masaryk University the instrument was operated at a beam current of 10 nA and an accelerating voltage of 15 kV, and at the NHM at 20 nA and 20 kV. Where possible the beam was defocused to a spot size of 5–10 μm to minimize beam-induced damage and thermal decomposition of fluorcarbonate phases. The

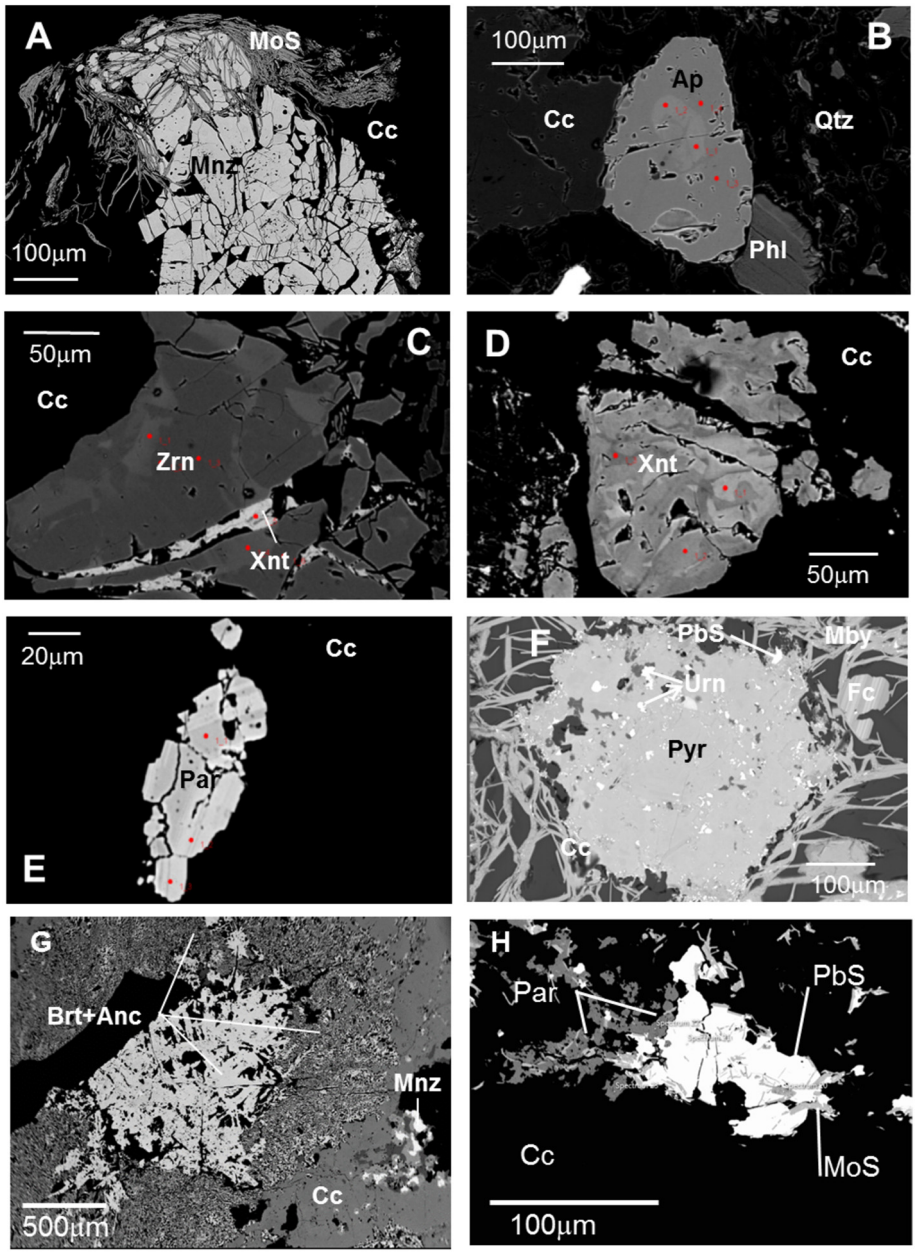


**Fig. 5.** Back scattered electron images of early magmatic phases. (A) Monazite within calcite carbonatite, with overgrowth and fracture fill of molybdenite. (B) Apatite in calcite-quartz carbonatite. (C) Zircon with xenotime fracture fill in calcite. (D) Isolated, patchily zoned xenotime in calcite. (E) Possibly primary parisite in calcite carbonatite. (F) Pyrochlore with uraninite inclusions overgrown by molybdenite, galena and REE fluorcarbonates, all in calcite carbonatite. (G) Backscattered electron image of intergrown barite and ancyltite in calcite carbonatite. The barite-ancylite intergrowth is inferred to represent a pseudomorph after early burbankite. (H) Association of parisite-(Ce) with galena and molybdenite. Mnz – monazite; Cc – calcite; Ap – apatite; Qtz – quartz; Phl – phlogopite; Zrn – zircon; Xnt – xenotime; Par – parisite; Pyr – pyrochlore; Urn – uraninite; PbS – galena; MoS – molybdenite; Fc – REE fluorcarbonate. Brt – barite; Anc - ancylite.

standards and emission lines used are summarised in E-Appendix 1, alongside typical detection limits for fluorcarbonate phases. The data were reduced and corrected using the PAP routine (Pouchou and Pichoir, 1984). Inter-element peak interferences, particularly for the REE, were corrected for by analysis of the pure standards following methods outlined by Williams (1996).

### 3.3. La-ICPMS

Trace-element analysis of selected carbonates, oxides and phosphates by laser-ablation inductively-coupled-plasma mass-spectrometry (LA-ICP-MS) was performed at the Laboratory of Atomic Spectrochemistry, Masaryk University, and the NHM, London using New-Wave UP-213 Frequency 348 quintupled Nd:YAG laser systems operated at a wavelength of 213 nm and pulse duration of 4.2 ns. At Masaryk an Agilent 7500ce spectrometer was used, and at the NHM an ICP-MS 349 – ThermoElemental PlasmaQuad III. Helium was used as a carrier gas with a flow rate of 1 l/min. The samples were analysed using a spot diameter of 25 or 30 μm, dwell time of 60 s, repetition rate of 10 Hz and fluence of 5 J/cm$^2$. The calcium content determined by WDS was used as an internal standard for all carbonates and phosphates, and external calibration was performed using glass standards NIST 610 and 612. For low Ca or Ca-free phases the internal standard used was Ce. Columbia River Basalt glass BCR2G was analysed as a quality check. Within run reproducibility of NIST612 analyses was typically within 1% of the published values, and of BCR2 within 5% of published values.

## 4. Results

### 4.1. Mineralogical evolution of the Huanglongpu system

The paragenetic evolution of the Huanglongpu system is summarised in Fig. 4 and the REE mineral assemblage is illustrated in Figs. 5 and 6. Early REE mineral crystallisation is characterised by the occurrence of sub- to euhedral monazite-(Ce), parisite-(Ce), bastnäsite-(Ce) and REE-bearing apatite (Fig. 5A, B). The REE are also hosted in zircon and xenotime (Fig. 5C, D). Xenotime is developed both as individual grains (Fig. 5D) and hosted in fractures in zircon (Fig. 5C). The patchy zonation

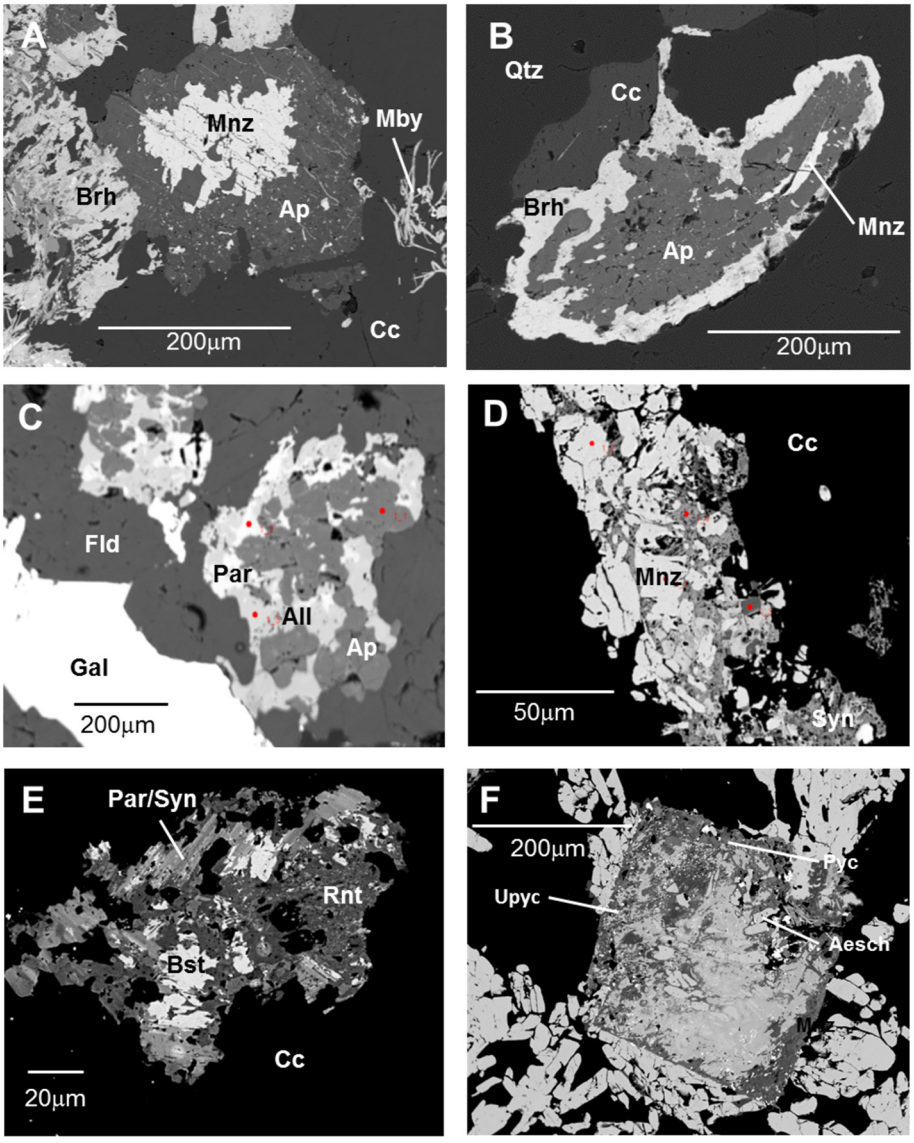


**Fig. 6.** Back scattered electron images of reaction textures showing the development of the secondary REE mineral assemblage. (A) Apatite corona developed on monazite associated with britholite in calcite carbonatite. (B) Britholite overgrowth and replacement of apatite with relict monazite in apatite core. In calcite-quartz carbonatite. (C) Allanite overgrowth on apatite, with subsequent overgrowth and replacement by parisite. (D) Synchysite overgrowth on monazite. (E) Bastnäsite replacement by parisite-synchysite syntaxial intergrowth. All are then replaced by röntgenite. (F) Alteration of aeschynite to uranopyrochlore and pyrochlore Abbreviations as Fig. 5, plus Brh – britholite; Fld – K-feldspar; Snc – synchysite; Rnt – röntgenite; Aesch – aeschynite; Upyc – uranopyrochlore; Pyc – pyrochlore; Urn – uraninite.

**Table 2**
Representative bulk rock analyses of Huanglongpu carbonatites. Data from Xu et al. (2010), Kynicky et al. (2012) and Song et al. (2015). LREE – La to Sm; HREE – Eu to Lu + Y.

| Sample | HLP-1 | HLP-3 | HLP-4 | HLP-5 | HLP-6 |
|---|---|---|---|---|---|
| *Major elements (weight %)* | | | | | |
| SiO2 | 1.18 | 1.56 | 1.07 | 1.27 | 4.26 |
| TiO2 | 0.08 | 0.10 | 0.09 | 0.07 | 0.18 |
| Al2O3 | 2.10 | 2.24 | 1.54 | 1.25 | 6.36 |
| Fe2O3 | 0.37 | 0.51 | 0.41 | 0.48 | 0.35 |
| MnO | 1.00 | 2.59 | 1.47 | 1.29 | 1.20 |
| MgO | 0.40 | 0.44 | 0.42 | 0.41 | 0.33 |
| CaO | 53.35 | 51.39 | 53.01 | 53.03 | 48.41 |
| Na2O | 0.08 | 0.15 | 0.08 | 0.09 | 0.18 |
| K2O | 0.18 | 0.06 | 0.04 | 0.02 | 1.03 |
| P2O5 | 0.04 | 0.05 | 0.03 | 0.03 | 0.05 |
| CO2 | 40.94 | 40.65 | 41.48 | 41.67 | 37.37 |
| Total | 99.71 | 99.74 | 99.63 | 99.61 | 99.72 |
| *Trace elements (ppm)* | | | | | |
| Rb | 3.0 | 0.9 | 0.4 | 0.3 | 5.8 |
| Ba | 912.0 | 154.0 | 184.0 | 197.0 | 510.0 |
| Th | 0.8 | 0.2 | 0.0 | 0.2 | 0.6 |
| U | 0.6 | 0.9 | 0.3 | 0.9 | 0.2 |
| Nb | 1.2 | 0.5 | 0.4 | 0.9 | 0.4 |
| Ta | 0.2 | 0.4 | 0.3 | 0.3 | 0.2 |
| La | 220.0 | 130.0 | 279.0 | 140.0 | 186.0 |
| Ce | 516.0 | 445.0 | 764.0 | 516.0 | 527.0 |
| Pr | 47.9 | 46.1 | 76.9 | 53.2 | 52.4 |
| Sr | 7753.0 | 6938.0 | 8441.0 | 7096.0 | 7957.0 |
| Nd | 200.0 | 210.0 | 336.0 | 240.0 | 230.0 |
| Sm | 41.7 | 58.2 | 71.9 | 60.1 | 50.9 |
| Zr | 0.4 | 0.4 | 0.3 | 0.2 | 29.3 |
| Hf | 0.2 | 0.5 | 0.3 | 0.4 | 0.8 |
| Eu | 11.3 | 17.9 | 18.6 | 17.2 | 13.5 |
| Gd | 38.0 | 61.2 | 60.7 | 56.8 | 45.5 |
| Tb | 5.7 | 11.3 | 8.8 | 9.5 | 6.8 |
| Dy | 34.3 | 77.4 | 49.6 | 59.7 | 41.6 |
| Y | 365.0 | 841.0 | 426.0 | 589.0 | 421.0 |
| Ho | 8.3 | 19.2 | 10.9 | 13.6 | 9.7 |
| Er | 28.6 | 67.3 | 34.2 | 44.9 | 32.9 |
| Tm | 4.9 | 11.8 | 5.2 | 7.5 | 5.5 |
| Yb | 35.3 | 86.0 | 34.7 | 53.0 | 37.9 |
| Lu | 5.6 | 13.3 | 4.8 | 8.1 | 5.6 |
| ΣREE | 1563 | 2096 | 2181 | 1869 | 1666 |
| HREE/LREE | 1.91 | 0.74 | 2.34 | 1.17 | 1.69 |

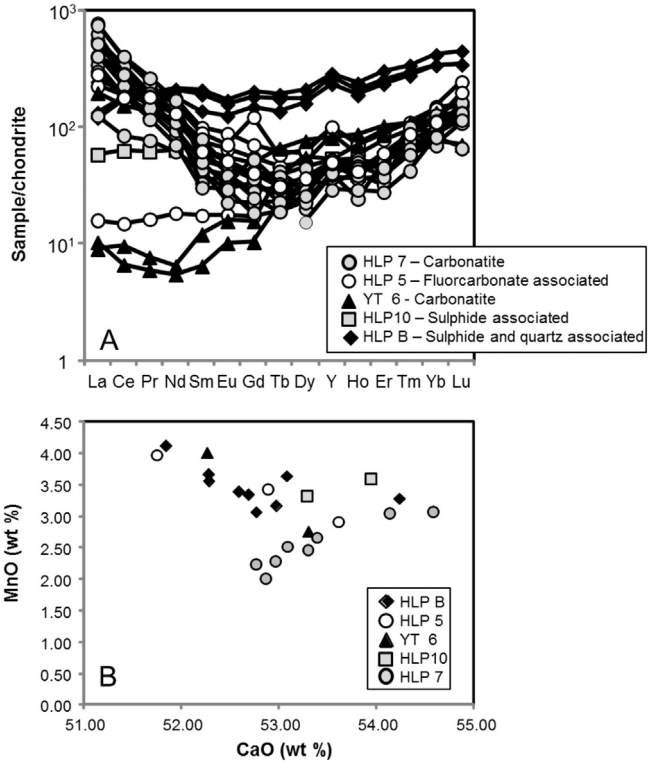


**Fig. 7.** (A) Chondrite normalised REE content of calcite from LA-ICPMS analyses. (B) MnO content of calcite from EPMA.

of xenotime (Fig. 5D) suggests it may have been subject to alteration and dissolution-reprecipitation processes. Xenotime was not studied in detail here as it does not constitute a major contributor to the HREE budget. Potentially primary parisite-(Ce) (indicated by the lack of alteration to other Ca-REE fluorcarbonates) occurs within the carbonate-dominant zone of the dykes (Fig. 5E) in association with sulphides. Early magmatic crystallisation also included the formation of Nb minerals, dominated by

**Table 3**
Representative major element (WDS and EDS) and trace element (LA-ICPMS) analyses of calcite.

| | LA-ICPMS DL# | HLPB | HLPB | HLP5 | HLP5 | YT6 | YT6 | HLP10 | HLP7 | HLP7 |
|---|---|---|---|---|---|---|---|---|---|---|
| *Major element concentration in weight %.* | | | | | | | | | | |
| Technique | | EDS | EDS | EDS | EDS | EDS | EDS | EDS | WDS | WDS |
| CaO | | 51.84 | 54.23 | 52.88 | 53.61 | 53.30 | 52.26 | 53.28 | 53.38 | 52.86 |
| MgO | | 0.51 | 0.00 | 0.31 | 0.31 | 0.12 | 0.00 | 0.00 | 0.40 | 0.28 |
| MnO | | 4.14 | 3.29 | 3.44 | 2.92 | 2.77 | 4.02 | 3.34 | 2.67 | 2.02 |
| FeO | | 0.53 | 0.00 | 0.29 | 0.00 | 0.81 | 1.17 | 0.00 | 0.29 | 0.28 |
| SrO | | 0.61 | 0.00 | 0.70 | 0.72 | 0.64 | 0.26 | 1.11 | 1.29 | 1.27 |
| *LA-ICPMS concentration in ppm.* | | | | | | | | | | |
| La | 0.03 | 29 | 59 | 4 | 95 | 2 | 47 | 14 | 30 | 152 |
| Ce | 0.03 | 107 | 132 | 9 | 169 | 6 | 96 | 39 | 53 | 179 |
| Pr | 0.03 | 17 | 19 | 2 | 20 | 1 | 13 | 6 | 7 | 18 |
| Nd | 0.31 | 97 | 83 | 8 | 73 | 3 | 53 | 29 | 29 | 43 |
| Sm | 0.17 | 29 | 21 | 3 | 13 | 2 | 9 | 6 | 7 | 8 |
| Eu | 0.06 | 9 | 7 | 1 | 4 | 1 | 3 | 2 | 2 | 3 |
| Gd | 0.24 | 37 | 30 | 3 | 25 | 3 | 10 | 7 | 6 | 8 |
| Tb | 0.03 | 6 | 5 | 1 | 2 | 1 | 2 | 1 | 1 | 1 |
| Dy | 0.14 | 44 | 40 | 6 | 16 | 14 | 19 | 7 | 8 | 5 |
| Y | 0.03 | 424 | 373 | 76 | 161 | 83 | 129 | 86 | 83 | 62 |
| Ho | 0.03 | 11 | 10 | 2 | 4 | 4 | 5 | 2 | 2 | 1 |
| Er | 0.15 | 42 | 38 | 9 | 15 | 14 | 17 | 9 | 5 | 8 |
| Tm | 0.03 | 7 | 7 | 2 | 3 | 3 | 3 | 2 | 2 | 2 |
| Yb | 0.14 | 55 | 55 | 25 | 23 | 22 | 19 | 16 | 15 | 13 |
| Lu | 0.02 | 9 | 9 | 6 | 4 | 3 | 3 | 3 | 4 | 3 |
| Th | 0.03 | BD[a] | BD[a] | BD[a] | BD[a] | BD[a] | BD[a] | BD[a] | BD[a] | BD[a] |
| U | 0.03 | BD[a] | BD[a] | BD[a] | BD[a] | BD[a] | BD[a] | BD[a] | BD[a] | BD[a] |

#DL - Detection Limit
[a] Below detection.

aeschynite-(Ce), but also including pyrochlore (Fig. 5F). Early stage magmatic crystallisation is also inferred to have included the formation of primary Na-Ba-Sr-REE carbonates of the burbankite group. Potential burbankite pseudomorphs are preserved as coarse grained, hexagonal pods (up to 2 cm in diameter) in-filled by barite, or a solid solution of barite-celestine, strontianite and ancylite (Fig. 5G). Burbankite has not been directly observed, but this texture and assemblage is typical of burbankite replacement (Zaitsev et al., 1998, 2002).

The subsequent development of the REE mineral paragenesis is recorded by reaction textures in phosphates and silicates, the colloform banded infill of niobate pseudomorphs, and the development of *syn*- to epitaxial alteration and overgrowth in the fluorcarbonates. The fluorcarbonate assemblage appears to be related to the formation of sulphides (notably galena and molybdenite; Fig. 5H). The earliest of these textures involves the partial replacement and overgrowth of monazite-(Ce) by REE-enriched apatite (Fig. 6A). The apatite is zoned, with more REE-depleted areas developed towards the outer rim of the coronae. The apatite is replaced in some instances by an outer layer of britholite-(Ce), sometimes giving multi-layered structures (Fig. 6B). Britholite-(Ce) is sometimes at the contact with quartz within the dyke cores. These outer layers are frequently associated with molybdenite. Potentially synchronous with the development of britholite-(Ce) is the formation of allanite-(Ce), which in some instances overgrows apatite. In at least one case this is associated with the development of later stage parisite-(Ce) (Fig. 6C), and Ca-REE-fluorcarbonates may overgrow all the preceding phases (e.g. Fig. 6D). The syntaxial intergrowth and epitaxial overgrowth patterns of the Ca-REE-fluorcarbonates allow a sequence of their formation to be determined, with early parisite-(Ce), sometimes intergrown with, and sometimes overgrown and partly replaced by, bastnäsite-(Ce). Parisite-(Ce) also occurs intergrown and overgrown by synchysite-(Ce), and ultimately all are overgrown and partially replaced by röntgenite-(Ce) (Fig. 6E). Synchysite-(Ce) and röntgenite-(Ce) are always enriched in Y relative to bastnäsite-(Ce) and parisite-(Ce), and in rare examples occur as the Y-dominant phase (synchysite-(Y)). Textures involving fluorcarbonate overgrowth are typically developed within calcite.

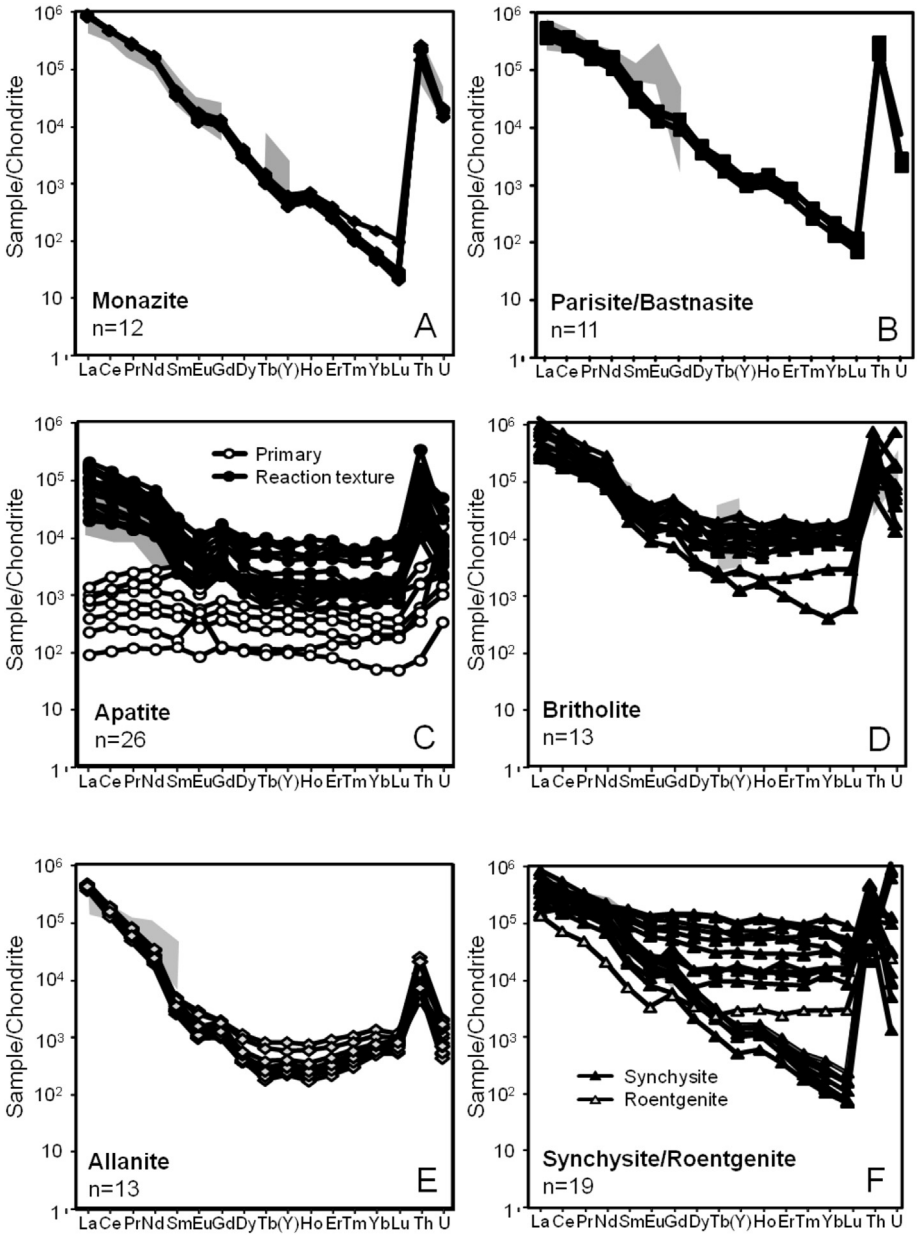


**Fig. 8.** Chondrite normalised REE + U + Th content of REE minerals. Grey shading indicates the range of analyses from corresponding EPMA spots. (a) Monazite. (b) Parisite and Bastnäsite. (c) Apatite subdivided by discrete grains (Primary) and apatite involved in reaction textures. (d) Britholite. (e) Allanite. (f) Synchysite and röntgenite.

The textural evolution of the niobium mineral paragenesis parallels that of the REE minerals. Euhedral pseudomorphs are commonly associated with monazite (Fig. 6F). The initial Nb phase seems to have been aeschynite-(Ce), on the basis of well crystalline, subhedral relicts within larger pseudomorphs (Fig. 6F). These early Nb-phases formed either synchronously with monazite, or pre-monazite crystallisation as indicated by the overgrowth of pseudomorphous aggregates of Nb-minerals by monazite-(Ce). Aeschynite-(Ce) is subsequently partially replaced by uranopyrochlore, and then both are replaced and overgrown by pyrochlore. The replacement of the primary aeschynite-(Ce) is accompanied by the development of uraninite inclusions (Fig. 6F).

### 4.2. REE geochemistry

The full results of LA-ICPMS and EPMA are available in Electronic Appendices 2 and 3. The results of LA-ICPMS and EPMA analyses are generally in good agreement for the LREE. Agreement is less good for the M-HREE and low levels of U and Th where concentrations approach the detection limit for EPMA for the conditions used. In these cases the LA-ICPMS data are the most accurate values. The values are compared in E-Appendix 3. Variation between EPMA and LA-ICPMS for corresponding points is a function of the relative volume analysed in each case, and the absolute precision of each technique. Low analytical totals for the fluorcarbonate minerals and niobate minerals occur in the EPMA data. In the case of the fluorcarbonates this is because a narrow beam diameter was used in order to analyse the fine intergrowth in some reaction textures, resulting in beam damage during analysis. In the case of the niobates low analytical totals are typical for EPMA analyses of pyrochlore and aeschynite because of their susceptibility to hydration and metamictisation (Lumpkin and Ewing, 1992, 1995).

The whole rock geochemistry of the Huanglongpu carbonatites is depleted in the LREE and enriched in the HREE compared to most carbonatite occurrences (Xu et al., 2010; Kynicky et al., 2012; Song et al., 2015; Table 2; Fig. 2). This is also reflected in the trace element chemistry of calcite (Table 3), which in the majority of the dykes shows relatively flat REE patterns, but may vary from LREE-enriched with flat HREE segments to strongly HREE-enriched (Fig. 7). This variation reflects variation in calcite generations, as HREE enriched patterns occur in calcite adjacent to the late stage Ca-REE fluorcarbonates. The REE patterns of REE-minerals and apatite show dramatic changes with evolution of the mineral paragenesis (Fig. 8; Tables 4-6). Both monazite-(Ce) (Table 4) and primary bastnäsite-(Ce) and parisite-(Ce) (Table 5) show strongly LREE-enriched patterns with very minor negative anomalies at Eu relative to Sm and Gd, and Y relative to Dy and Ho (Fig. 8A, B). Primary apatite (Table 4) shows relatively flat to upwards convex patterns with variably negative or positive Eu anomalies. In contrast secondary apatite in coronas around monazite is LREE-enriched, with flat HREE patterns from Dy to Lu and a consistently negative Eu anomaly (Fig. 8C). Similar patterns, albeit at higher absolute concentration, are observed in britholite and allanite (Fig. 8D, E; Table 6). Secondary REE-fluorcarbonate minerals either show patterns comparable to primary bastnäsite-(Ce) and parisite-(Ce), or show very strong HREE-enrichment, most notably in synchysite-(Y) replacing earlier phases, and in röntgenite (Fig. 8F; Table 5).

For economic considerations it is also important to quantify the behaviour of U and Th in the REE phases and during the development of the paragenesis. This is important as enrichment of the HREE may be characteristically accompanied by enrichment in U, and particularly in Th (e.g. Lofdal, Namibia; Wall et al., 2008; and Tundulu, Malawi; Broom-Fendley et al., 2016). For this reason chondrite normalised

**Table 4**
Representative analyses of monazite (M) and apatite (A) by electron microprobe (EPMA) and LA-ICPMS.

| | EPMA DL wt% | LA-ICPMS DL | HLP1 M-Grain | HLP10 M-Corona | HLP-B M-Grain | HLP15 M-Grain | HLP7 M-Corona | YT2 M-Grain | YT1 M-Grain | HLP10 A-Corona | HLP10 A-Corona Rim | HLP-A A-Grain |
|---|---|---|---|---|---|---|---|---|---|---|---|---|
| CaO | 0.03 | | 0.16 | 0.87 | 0.19 | 0.21 | 0.18 | 1.10 | 0.38 | 49.12 | 52.79 | 55.13 |
| SrO | 0.05 | | B.D. | B.D. | B.D. | B.D. | B.D. | B.D. | B.D. | 0.71 | 0.59 | B.D. |
| MnO | 0.03 | | B.D. | B.D. | B.D. | B.D. | B.D. | B.D. | B.D. | 0.23 | 0.10 | 0.06 |
| La2O3 | 0.08 | | 19.17 | 20.77 | 22.04 | 22.43 | 21.17 | 20.85 | 21.87 | 1.27 | 0.69 | B.D. |
| Ce2O3 | 0.10 | | 32.74 | 33.48 | 34.22 | 34.85 | 34.99 | 34.19 | 33.25 | 2.64 | 1.34 | B.D. |
| Pr2O3 | 0.16 | | 3.06 | 2.54 | 2.80 | 2.79 | 3.137 | 2.85 | 2.79 | 0.27 | 0.09 | B.D. |
| Nd2O3 | 0.08 | | 9.82 | 7.77 | 8.01 | 8.08 | 8.45 | 8.44 | 8.06 | 0.84 | 0.32 | B.D. |
| Sm2O3 | 0.04 | | 1.04 | 0.52 | 0.55 | 0.66 | 0.72 | 0.65 | 0.66 | 0.10 | B.D. | B.D. |
| ThO2 | 0.09 | | 1.00 | 0.77 | 0.62 | 0.27 | 0.45 | 0.35 | 0.43 | B.D. | B.D. | B.D. |
| SiO2 | 0.03 | | 0.19 | 0.80 | 0.57 | BD | 0.53 | 0.56 | 0.55 | 2.07 | 0.43 | 0.34 |
| P2O5 | 0.03 | | 28.63 | 26.59 | 28.10 | 29.60 | 29.32 | 28.14 | 28.28 | 34.79 | 38.76 | 40.74 |
| F | 0.08 | | B.D. | B.D. | B.D. | B.D. | B.D. | B.D. | B.D. | 4.40 | 5.20 | 5.38 |
| Total | | | 95.81 | 94.11 | 97.10 | 98.89 | 98.95 | 97.13 | 96.27 | 96.80 | 100.30 | 101.91 |
| O=F | | | | | | | | | | 1.83 | 2.14 | 2.27 |
| Total | | | 95.81 | 94.11 | 97.10 | 98.89 | 98.95 | 97.13 | 96.27 | 94.97 | 98.16 | 99.65 |
| | ppm | ppm | EPMA | EPMA | LA-ICPMS | EPMA | EPMA | EPMA | EPMA | LA-ICPMS | LA-ICPMS | LA-ICPMS |
| La | 701 | 0.01 | 160,600 | 177,100 | 220,300 | 191,300 | 180,500 | 177,800 | 186,500 | 13,200 | 9250 | 51 |
| Ce | 867 | 0.01 | 279,500 | 285,800 | 291,700 | 297,500 | 298,700 | 291,900 | 283,800 | 27,400 | 19,300 | 161 |
| Pr | 1325 | 0.01 | 26,100 | 21,700 | 26,600 | 23,800 | 26,800 | 24,400 | 23,900 | 2800 | 1950 | 22 |
| Nd | 723 | 0.07 | 84,200 | 66,600 | 77,900 | 69,200 | 72,400 | 72,400 | 69,100 | 8550 | 6140 | 94 |
| Sm | 368 | 0.04 | 8980 | 4500 | 5920 | 5670 | 6200 | 5560 | 5700 | 862 | 755 | 23 |
| Eu | 151 | 0.01 | BD[a] | BD | 920 | BD | 560 | BD | BD | 159 | 165 | 27 |
| Gd | 66 | 0.04 | 4900 | BD | 2560 | BD | 1750 | BD | 2350 | 448 | 579 | 22 |
| Tb | | 0.01 | NA | NA | 141 | NA | 600 | NA | NA | 38 | 67 | 4 |
| Dy | 1223 | 0.03 | BD | BD | 334 | BD | BD | BD | BD | 159 | 448 | 26 |
| Y | 1071 | 0.01 | 5800 | BD | 883 | BD | BD | BD | BD | 1190 | 2502 | 164 |
| Ho | | 0.01 | NA[b] | NA | 34 | NA | NA | NA | NA | 30 | 85 | 6 |
| Er | 1309 | 0.03 | BD | BD | 49 | BD | BD | BD | BD | 95 | 252 | 21 |
| Tm | | 0.01 | NA | NA | 3 | NA | NA | NA | NA | 14 | 39 | 3 |
| Yb | 843 | 0.04 | BD | BD | 9 | BD | BD | BD | BD | 114 | 267 | 30 |
| Lu | 679 | 0.01 | BD | BD | 1 | BD | BD | BD | BD | 18 | 35 | 5 |
| Th | 786 | 0.01 | 8770 | 6755 | 5980 | BD | BD | BD | BD | 16,054 | 5470 | 10 |
| U | 1492 | 0.01 | BD | BD | 110 | BD | BD | BD | BD | 49 | 135 | 114 |

# DL - Detection Limit.
[a] Below detection.
[b] Not analysed.

**Table 5**
Representative analyses of REE fluorcarbonates by electron microprobe (EPMA) and LA-ICPMS. Mineral abbreviations as in Table 1.

| | EPMA DL# | LA-ICPMS DL | YT6 | | HLP5 | | | | HLP6 | | HLP15 | | | YT2 |
|---|---|---|---|---|---|---|---|---|---|---|---|---|---|---|
| | wt% | | Par | Rnt | Bst | Par | Rnt | Syn | Bst | Syn | Par | Rnt | Syn | Bst |
| CaO | 0.03 | | 10.15 | 16.41 | 0.23 | 9.92 | 13.01 | 16.50 | 0.05 | 17.76 | 9.72 | 15.75 | 21.23 | 0.10 |
| FeO | 0.03 | | BD | BD | 0.00 | BD | 0.00 | 1.44 | BD | BD | BD | BD | BD | BD |
| SrO | 0.07 | | 0.75 | 0.60 | 0.07 | 0.09 | 0.06 | 0.06 | <dt | 0.05 | BD | BD | BD | BD |
| Y2O3 | 0.04 | | 0.32 | 0.13 | 0.41 | 1.42 | 1.30 | 6.17 | BD | 3.29 | 0.76 | 0.50 | 0.94 | 0.32 |
| La2O3 | 0.05 | | 18.78 | 13.83 | 14.91 | 11.00 | 12.73 | 7.22 | 23.66 | 9.29 | 13.02 | 8.82 | 7.52 | 18.87 |
| Ce2O3 | 0.07 | | 30.10 | 26.52 | 34.28 | 26.11 | 23.32 | 18.70 | 33.66 | 20.88 | 27.21 | 20.31 | 18.43 | 30.10 |
| Pr2O3 | 0.10 | | 2.67 | 2.54 | 3.49 | 3.09 | 2.65 | 2.28 | 2.67 | 2.30 | 2.80 | 2.33 | 2.34 | 2.67 |
| Nd2O3 | 0.05 | | 9.23 | 8.15 | 12.01 | 11.80 | 10.04 | 8.60 | 8.19 | 9.31 | 10.74 | 9.77 | 8.80 | 9.23 |
| Sm2O3 | 0.03 | | 0.98 | 0.73 | 1.44 | 2.06 | 2.06 | 1.66 | 0.55 | 2.10 | 1.25 | 1.15 | 1.47 | 0.98 |
| SiO2 | 0.03 | | 0.16 | 0.14 | 0.131 | 0.11 | 13.28 | 0.13 | 0.13 | 0.08 | 0.20 | 0.33 | 0.30 | 0.10 |
| F | 0.04 | | 5.43 | 4.70 | 6.982 | 4.91 | 3.39 | 4.03 | 7.12 | 3.93 | 4.45 | 4.69 | 4.67 | 6.86 |
| | ppm | ppm | LA | LA | EPMA | LA | EPMA | LA | EPMA | EPMA | EPMA | EPMA | EPMA | EPMA |
| La | 591 | 0.03 | 85,000 | 202,500 | 127,200 | 75,900 | 108,500 | 63,900 | 201,800 | 79,200 | 111,000 | 75,200 | 64,100 | 190,000 |
| Ce | 875 | 0.02 | 156,200 | 338,600 | 292,700 | 144,600 | 199,000 | 159,800 | 287,300 | 179,200 | 232,200 | 173,300 | 157,300 | 310,500 |
| Pr | 1187 | 0.01 | 14,200 | 32,100 | 29,800 | 17,700 | 22,600 | 20,000 | 22,800 | 19,700 | 23,900 | 19,900 | 20,000 | 25,300 |
| Nd | 669 | 0.26 | 46,900 | 104,300 | 102,900 | 71,600 | 86,200 | 87,900 | 70,200 | 79,800 | 92,100 | 83,800 | 75,500 | 75,700 |
| Sm | 437 | 0.22 | 4120 | 9270 | 12,450 | 11,600 | 17,700 | 19,200 | 4710 | 1810 | 10,800 | 9900 | 12,700 | 4500 |
| Eu | 151 | 0.05 | 717 | 1550 | 3500 | 2460 | 13,000 | 4700 | BD[a] | 17,600 | 2300 | BD | 750 | 1100 |
| Gd | 29 | 0.10 | 1830 | 4040 | 1300 | 7640 | 3300 | 17,400 | 1300 | 6600 | 4800 | 5000 | 5990 | 1550 |
| Tb | | 0.02 | 131 | 245 | NA[b] | 915 | BD | 2750 | BD | BD | BD | BD | BD | BD |
| Dy | 1255 | 0.07 | 488 | 795 | BD | 5040 | BD | 15,900 | BD | BD | BD | BD | BD | BD |
| Y | 328 | 0.02 | 1500 | 2360 | 3200 | 27,300 | 10,200 | 113,300 | BD | 25,900 | 6000 | 3900 | 7400 | 840 |
| Ho | | 0.01 | 62 | 91 | NA | 978 | NA | 3920 | NA | NA | NA | NA | NA | NA |
| Er | 1247 | 0.09 | 98 | 150 | BD | 2650 | NA | 13,200 | BD | BD | BD | BD | BD | BD |
| Tm | | 0.02 | 6 | 11 | NA | 429 | NA | 2320 | NA | NA | NA | NA | NA | NA |
| Yb | 663 | 0.14 | 21 | 47 | 342 | 2760 | NA | 19,500 | BD | 817 | BD | BD | BD | BD |
| Lu | 626 | 0.03 | 2 | 4 | BD | 353 | NA | 2260 | BD | BD | BD | BD | BD | BD |
| Th | 763 | 0.02 | 5370 | 13,500 | 176 | 673 | NA | 1570 | 4570 | 4570 | BD | 13,867 | 475 | BD |
| U | 1394 | 0.02 | 16 | 38 | BD | 1030 | NA | 6520 | BD | BD | BD | BD | BD | BD |

# DL - Detection Limit.
[a] Below detection.
[b] Not analysed.

U and Th concentrations are plotted alongside the REE in Fig. 8. In all cases Th is significantly enriched relative to U and the HREE, except for in the secondary Ca-REE fluorcarbonates. In late stage synchysite and röntgentite the pattern is reversed, and Th is relatively depleted. The absolute variation in U and Th content is shown in Tables 4-7.

For apatite and britholite-(Ce) the principle substitution leading to REE incorporation is of the form $[Ca^{2+}]^{-1}[P^{5+}]^{-1}[REE^{3+}][Si^{4+}]$. In allanite ΣREE is consistently close to 1 a.p.f.u. (atoms per formula unit), but variation of the Fe:Al ratio indicates development of a ferri-allanite substitution, and $Fe^{3+}$ dominant within the allanite structure. In some instance more Mn-rich allanites are developed (Table 6). Formulae calculations (E-Appendix 2) suggest there is an excess of F over stoichiometric amounts in some apatite analyses. This is accompanied by a deficiency in P, suggesting a francolite (carbonate apatite) component, although there may be issues with F mobility under the electron beam. Theoretical carbonate contents based on the P deficiency are calculated in E-Appendix 2, but are only indicative concentrations as they assume a full phosphate site occupancy.

The niobates within the Huanglongpu district are consistently Nb-rich with minimal Ta content (Fig. 9A, B; Table 7). Compositions show a continuous transition between aeschynite-(Ce) and pyrochlore, with limited development of an A-site vacancy (Fig. 9C). Primary aeschynite-(Ce) has relatively low U contents, whilst pyrochlore shows a continuous variation in U content (Fig. 9D). In terms of REE pattern aeschynite-(Ce) is consistently LREE enriched, and the REE patterns is comparable to monazite-(Ce) and bastnäsite-(Ce) (Fig. 10A). The very fine nature of the banding in the replacement products of aeschynite-(Ce) restricted the applicability of LA-ICPMS, hence the analyses completed are dominantly by electron microprobe. The occurrence of a limited number of coarse uranopyrochlore grains allowed some analyses (Fig. 10B). These show that alteration of uranopyrochlore to pyrochlore resulted in a relative enrichment in the HREE. The transition from aeschynite-(Ce) to uranopyrochlore shows a slope of ~0.5 on a plot of ΣREE vs U, and is consistent with REE leaching and the addition of U during alteration according to the substitution $[REE^{3+}]^{-2}[U^{4+}][Ca^{2+}]$ (Fig. 10C).

## 5. Discussion

### 5.1. The evolution of the Huanglongpu REE mineralisation

The mineralogical evolution of the Huanglongpu REE system reflects that of the host carbonatite. The primary REE mineralogy consists of monazite and bastnäsite, with phases with no essential REE contributing to the HREE budget (apatite and zircon). A major contribution to the primary REE budget may have come from the presence of burbankite, now pseudomorphed by ancylite and barite. Early Nb mineralisation appears to have been dominated by aeschynite, followed by replacement by uranopyrochlore and finally pyrochlore. The formation of a REE-rich A-B oxide at this stage relates to similar melt compositions to those during monazite deposition. The saturation of carbonatite melts in monazite and basnästite is typically related to passive enrichment on fractional crystallisation (Le Bas, 1987; Mitchell, 2005) which is a likely factor in this case (Xu et al., 2007). Aeschynite-(Ce) saturation in melts has not been specifically addressed in the literature, but the formation of Nb-minerals in general has been related to saturation following crystal fractionation, magma mixing, and redistribution of Nb-minerals by density currents (Mitchell, 2015). The reduction in niobate REE content through the paragenesis mirrors the reduction seen in phosphates and may reflect a similar process of fractional crystallisation and potentially REE-loss to a fluid phase.

The further development of the REE paragenesis features the overgrowth of monazite by REE-bearing apatite. Assuming a fixed phosphate framework (an assumption supported by the overall mineralogical change and data on phosphate mineral solubility – Tropper et al., 2011) this implies an increase in $a_{Ca^{2+}}$ and $a_{HF}$ in the surrounding fluids

**Table 6**
Representative analyses of REE silicates by electron microprobe (EPMA) and LA-ICPMS.

| | EPMA DL | LA-ICPMS DL | HLP 10 | | | | HLP11 | |
|---|---|---|---|---|---|---|---|---|
| | wt% | ppm | Britholite | Britholite | Allanite | Allanite | Allanite | Allanite |
| *Major elements by EPMA* | | | | | | | | |
| CaO | 0.03 | | 11.59 | 12.06 | 8.69 | 8.66 | 9.99 | 11.05 |
| MgO | 0.02 | | BD[a] | BD | 4.65 | 4.76 | 0.85 | 1.07 |
| MnO | 0.04 | | 0.68 | 0.58 | 6.72 | 6.42 | 1.49 | 1.46 |
| Fe2O3 | 0.03 | | BD | BD | 5.03 | 4.63 | 23.01 | 21.49 |
| Al2O3 | 0.02 | | BD | BD | 12.51 | 12.68 | 10.45 | 11.83 |
| SiO2 | 0.03 | | 19.42 | 18.50 | 30.28 | 30.30 | 29.96 | 30.70 |
| La2O3 | 0.08 | | 18.07 | 15.91 | 13.51 | 13.24 | 6.56 | 4.25 |
| Ce2O3 | 0.10 | | 31.71 | 29.31 | 12.62 | 12.50 | 10.79 | 9.94 |
| Pr2O3 | 0.15 | | 2.67 | 2.72 | 0.7 | 0.7 | 1.14 | 1.23 |
| Nd2O3 | 0.08 | | 8.15 | 8.17 | 1.30 | 1.30 | 4.27 | 4.27 |
| Sm2O3 | 0.02 | | 0.63 | 0.80 | BD | BD | 0.65 | 0.65 |
| Eu2O3 | 0.02 | | BD | BD | BD | BD | BD | BD |
| Gd2O3 | 0.01 | | BD | 0.24 | BD | BD | 0.34 | 0.38 |
| Dy2O3 | 0.14 | | BD | 0.25 | BD | BD | 0.05 | 0.08 |
| TiO2 | 0.03 | | BD | BD | 0.51 | 0.49 | 0.20 | 0.41 |
| P2O5 | 0.02 | | 1.44 | 2.14 | BD | BD | BD | BD |
| F | 0.05 | | 2.70 | 2.75 | 1.45 | 1.43 | 0.23 | 0.29 |
| Total | | | 98.23 | 96.77 | 97.96 | 97.11 | 100.43 | 100.39 |
| O = F | | | 2.09 | 2.09 | 2.09 | 2.09 | 2.09 | 2.09 |
| Total | | | 96.15 | 94.68 | 95.87 | 95.02 | 98.34 | 98.30 |
| *Trace elements by LA-ICPMS* | | | | | | | | |
| La | | 0.02 | 158,400 | 147,500 | 94,000 | 107,600 | 102,000 | 111,000 |
| Ce | | 0.04 | 101,500 | 260,600 | 91,300 | 100,500 | 112,400 | 105,800 |
| Pr | | 0.03 | 10,900 | 26,600 | 5740 | 5940 | 7430 | 6450 |
| Nd | | 0.38 | 35,700 | 91,000 | 11,700 | 11,900 | 15,200 | 12,300 |
| Sm | | 0.33 | 4170 | 9290 | 719 | 709 | 565 | 461 |
| Eu | | 0.04 | 956 | 2050 | 160 | 140 | 77.4 | 61 |
| Gd | | 0.13 | 2810 | 5710 | 386 | 373 | 317 | 293 |
| Tb | | 0.03 | 326 | 682 | 40 | 32.8 | 14.1 | 14 |
| Dy | | 0.15 | 1840 | 3800 | 199 | 153 | 42.7 | 50 |
| Y | | 0.03 | 12,200 | 25,500 | 1270 | 869 | 337 | 378 |
| Ho | | 0.03 | 405 | 820 | 40 | 31 | 9.09 | 11 |
| Er | | 0.16 | 1220 | 2540 | 143 | 105 | 33.4 | 41 |
| Tm | | 0.03 | 183 | 379 | 26 | 20 | 7.21 | 9 |
| Yb | | 0.20 | 1350 | 2760 | 212 | 160 | 75.7 | 89 |
| Lu | | 0.03 | 182 | 332 | 28 | 22.8 | 13.6 | 16 |
| Th | | 0.10 | 3040 | 5360 | 250 | 248 | 164 | 367 |
| U | | 0.06 | 1250 | 5160 | 4 | 5 | 10.8 | 14 |

# DL - Detection Limit.
[a] Below detection.

(where a is activity), and a decrease in $a_{REE^{3+}}$. That this shift resulted in a decrease in $a_{REE^{3+}}$ probably reflects decline in melt REE content with early crystallisation of monazite and REE-rich niobates. The $a_{HF}$ never reached the point of widespread fluorite saturation, and may have been buffered to low levels by the formation of fluorapatite.

The subsequent paragenetic stage is the formation of britholite-(Ce), and by inference allanite-(Ce), reflecting increasing $a_{SiO_2}$ in the mineralising fluid. This is most clearly marked in the overall paragenetic evolution of the system by the formation of the quartz-rich cores to the dykes (Kynicky et al., 2012; Song et al., 2015; Xu et al., 2010). This stage can be unequivocally related to the initiation of hydrothermal conditions as fluid inclusion studies (Cangelosi, 2016; Song et al., 2015) indicate the presence of primary, sulphate-rich brines. Early aqueous-carbonic fluid inclusions with sulphate daughter minerals contain nearly pure $CO_2$, and have salinities in the aqueous phase determined from clathrate melting of 5–19 wt% NaCl equivalent (Wt% NaCl eq.). These inclusion decrepitate on heating, and so homogenisation temperatures cannot be determined. However, they occur in assemblages with liquid $CO_2$ inclusions, suggesting aqueous-carbonic fluid immiscibility during trapping (Cangelosi, 2016). In a 20 wt% salt fluid, below 100 MPa $XCO_2$ in the water-rich fluid during immiscibility is negligible, and below 50 MPa in a 5 wt% salt fluid. For both salinities there should be significant water in the $CO_2$-rich fluid above 200–300 °C (Bowers and Helgeson, 1983). This suggests that these inclusions were trapped between 300 and 200 °C and 100-50 MPa. Fluid inclusions in fracture-fill quartz and calcite are typically 2 phase aqueous liquid plus vapour inclusions. These homogenise between 265 and 120 °C, and have salinities from 6 to 15 wt% NaCl eq. Thus hydrothermal quartz deposition and the alteration of REE minerals took place from 300 to 120 °C, at pressures below 100 MPa, from saline brines that evolved from aqueous-carbonic compositions to aqueous-dominated compositions.

The final stage in the REE mineral evolution is the formation of Ca-REE fluorcarbonates overgrowing all REE-phases and replacing bastnäsite. This reflects increasing $a_{Ca^{2+}}$ and $a_{CO_3^{2-}}$ in the hydrothermal fluid, and has been linked to decreasing T in many systems (Smith et al., 2000; Williams-Jones and Wood, 1992). However, Gysi and Williams-Jones (2015) have demonstrated that the compositional field of bastnäsite stability increases with cooling at constant $a_{Ca^{2+}}$ in the system $REE_2O_3$-$CaF_2$-$CaCO_3$, so a change in fluid chemistry is necessary for the replacement reactions to develop (Fig. 11). This is most likely achieved as the fluid cools, with the resulting dissociation of acid species (e.g. HCl, $H_2SO_4$) and a corresponding drop in pH resulting in calcite dissolution.

### 5.2. Element mobility during sub-solidus metasomatism

At each alteration stage identified above there is a marked change in REE pattern. Fig. 12 shows the composition of alteration phases normalised to the precursor phase, modified by factors to allow for likely reaction stoichiometry assuming a fixed framework of either phosphate, carbonate or oxide.

**Table 7**
Representative analyses of Niobium minerals by electron microprobe (EPMA) and LA-ICPMS. Tantalum was included in all analyses but was below detection limits and so is not shown in the table.

| | EPMA DL | LA-ICPMS DL | HLP 15 Uranopyc | Pyc | YT2 Aesch | Aesch | Aesch | HLP11 Uranopyc | Uranopyc |
|---|---|---|---|---|---|---|---|---|---|
| | wt% | | EPMA | EPMA | EPMA | EPMA | EPMA | LA | LA |
| CaO | 0.03 | | 3.11 | 1.85 | 1.82 | 2.24 | 3.20 | 2.8[c] | 2.8[c] |
| SrO | 0.11 | | BD[a] | BD | 0.76 | 0.53 | 0.60 | 1.36 | 1.22 |
| MnO | 0.05 | | 0.38 | 0.21 | 0.20 | BD | BD | 0.35 | 0.36 |
| FeO | 0.04 | | 1.23 | 12.70 | 1.35 | 0.47 | 0.27 | 1.54 | 1.48 |
| TiO2 | 0.03 | | 22.22 | 29.61 | 14.32 | 12.07 | 6.27 | 22.52 | 21.46 |
| Nb2O5 | 0.13 | | 28.66 | 42.23 | 24.35 | 16.39 | 13.61 | 22.41 | 21.85 |
| SiO2 | 0.03 | | 2.65 | 0.75 | 0.47 | 0.60 | 0.52 | 1.47 | 1.28 |
| UO2 | 0.14 | | 30.14 | 1.95 | 20.09 | 18.02 | 11.78 | 26.22 | 18.44 |
| P2O5 | 0.02 | | BD[a] | 0.04 | 7.16 | 4.50 | 16.00 | NA[b] | NA[b] |
| F | 0.04 | | 0.11 | BD[a] | 0.27 | 2.18 | 0.50 | NA[b] | NA[b] |
| Total | | | 90.42 | 91.39 | 93.59 | 89.49 | 95.83 | 78.67 | 68.89 |
| | ppm | ppm | EPMA | EPMA | EPMA | EPMA | EPMA | LA-ICPMS | LA-ICPMS |
| La | 656 | 0.02 | BD | BD | 54,000 | 71,000 | 11,000 | 3492 | 3247 |
| Ce | 743 | 0.04 | 3280 | 2910 | 98,690 | 141,000 | 187,800 | 13,365 | 12,258 |
| Pr | 1290 | 0.03 | BD | BD | 8850 | 13,100 | 15,900 | 1854 | 1668 |
| Nd | 764 | 0.38 | 3900 | BD | 28,060 | 41,000 | 48,100 | 10,914 | 9566 |
| Sm | 487 | 0.33 | 730 | BD | 3000 | 4900 | 4100 | 1750 | 1486 |
| Eu | 168 | 0.04 | BD | BD | BD | BD | BD | 401 | 371 |
| Gd | 53 | 0.13 | 1300 | BD | BD | 950 | BD | 1303 | 1039 |
| Tb | | 0.03 | NA[b] | NA[b] | NA[b] | NA[b] | NA[b] | 154 | 117 |
| Dy | 1183 | 0.15 | BD | BD | BD | 1600 | BD | 1618 | 1193 |
| Y | 863 | 0.03 | BD | 2090 | 1600 | 3800 | BD | 3529 | 3300 |
| Ho | | 0.03 | NA[b] | NA[b] | NA[b] | NA[b] | NA[b] | 239 | 167 |
| Er | 1286 | 0.16 | BD | BD | BD | BD | BD | 1151 | 813 |
| Tm | | 0.03 | NA[b] | NA[b] | NA[b] | NA[b] | NA[b] | 118 | 86 |
| Yb | 824 | 0.20 | BD | BD | BD | BD | BD | 1254 | 902 |
| Lu | 654 | 0.03 | BD | BD | BD | BD | BD | 85 | 57 |
| Th | 803 | 0.10 | BD | BD | BD | BD | 3322 | 1017 | 847 |

# DL - Detection Limit.
[a] Below detection.
[b] Not analysed.
[c] Analyses from HLP 11 by LA-ICPMS and normalised to a mean Ca content of 2000 ppm.

The early alteration of monazite to apatite can be represented by Eq. (1):

$$3REEPO_4 + 5Ca^{2+} + F^- = Ca_5(PO_4)_3F + 3REE^{3+} \quad (1)$$

Monazite Apatite

Consideration of both reaction stoichiometry and the mineral chemistry indicates that the REE must have been significantly mobilised during this phase of alteration, and Fig. 12A indicates the leaching of the L-MREE (La-Ho), but addition of the lower abundance HREE (Er to Lu). Yttrium behaves anomalously, being enriched relative to Dy and Ho (Fig. 12A). Further alteration is visible on the rims of apatite coronas around monazite, and again indicates selective leaching of the LREE and immobility or passive enrichment of the HREE (Fig. 12B).

It is likely that the alteration of early aeschynite to uranopyrochlore and ultimately pyrochlore (Eqs. (2)-(3)) plus uraninite also occurred at this stage, as it also marks progressive depletion of a primary phase in the REE. It also implies an increase in fluid F-activities, as for alteration of monazite to apatite. Throughout this process alteration primarily affects the more mobile A-site cations (Ecrit, 2005; Lumpkin and Ewing, 1992, 1995, 1996), leaving a relatively unaltered B-site oxide framework. As with monazite alteration, REE leaching is restricted to the LREE (La-Eu), with relative immobility of the HREE (Fig. 12C).

$$(REE, Ca)(Ti, Nb)_2O_6 + F^- + U^{4+} = (U, Ca, REE)_2(Nb, Ti)_2O_6(F) + REE^{3+} \quad (2)$$

Aeschynite Uranopyrochlore

$$(U, Ca, REE)_2(Nb, Ta)_2O_6(F) = Ca_2Nb_2O_6(F) + UO_2 + REE^{3+} \quad (3)$$

Uranopyrochlore Pyrochlore

In both these cases the initial metasomatism is likely to be at the late magmatic stage. Fluorite is not common in the paragenesis, as would be expected for the interaction of an aqueous F-rich fluid with pre-existing calcite, which would also buffer F-species activities to low levels in any hydrothermal fluid. The alteration of uranopyrochlore to pyrochlore plus uraninite is likely to reflect hydrothermal alteration, however, with the relative immobility of U reflecting low $fO_2$ as implied by the sulphide mineral paragenesis (Fig. 12D).

The alteration of apatite to britholite requires mobile framework ions (Eq. (4)). Phosphate mobility from apatite via alteration to britholite requires low pH, and high $SiO_4^{4-}$ activities.

$$Ca_5(PO_4)_3F + 3SiO_4^{4-} + 3REE^{3+} = REE_3Ca_2(SiO_4)_3F + 3Ca^{2+} + 3PO4^{3-} \quad (4)$$

Apatite Britholite

This is indicative of a shift to full hydrothermal conditions, and accompanies the formation of quartz cores to dykes. The product to precursor normalised REE patterns of britholite-(Ce) vary (Fig. 12E), typically indicating either no fractionation of the REE during alteration of apatite, or preferential addition of the HREE. The assumption of a fixed crystallographic framework with substitution of $SiO_4^{4-}$ for $PO_4^{3-}$ implies no significant volume change on replacement. The actual mechanism of apatite replacement is likely to involve some component of dissolution-reprecipitation, which would generate some microporosity (Putnis, 2002) evident in apatite, but the factor of 10–20 increase in REE would require a much more significant volume reduction without a metasomatic REE flux. This is also supported by the formation of neoformed allanite around apatite, with comparable REE patterns to britholite. The textural evidence therefore favours metasomatic addition of the REE.

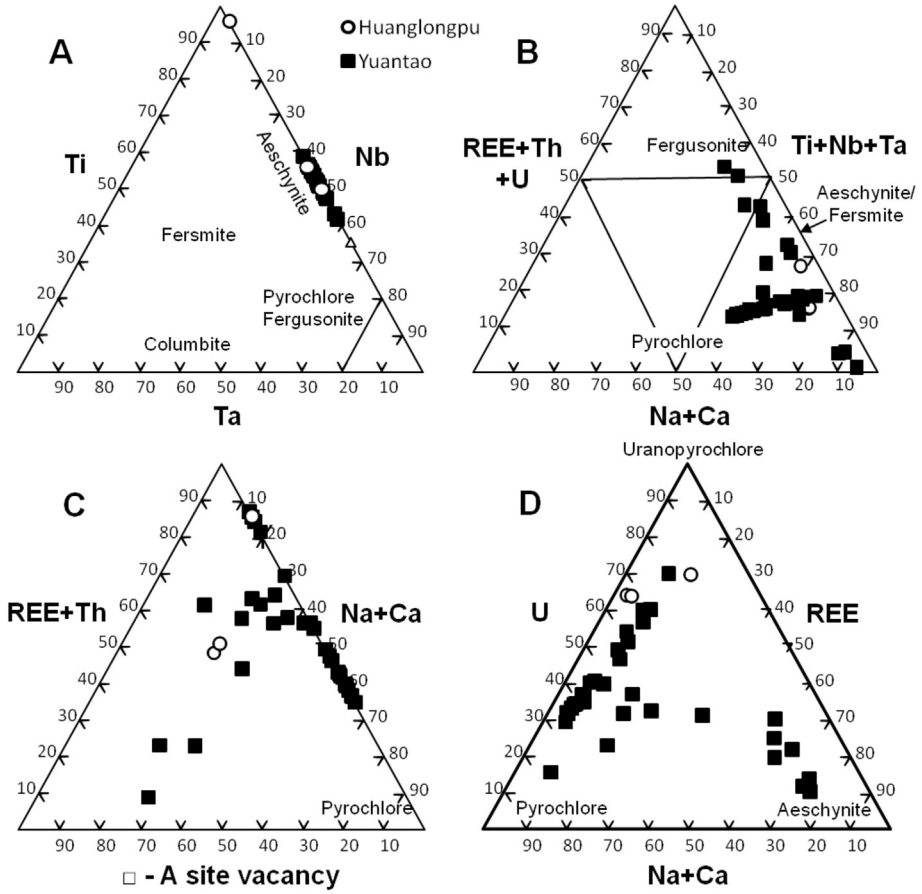


**Fig. 9.** Ternary diagrams in atomic % showing the major element composition of niobium minerals. A-site vacancy calculated on the basis of 6 oxygens. (a) B-site cations. (b) All major cations. (c) Major A-site cations. (d) Uranium and A-site cations.

The textural record of the fluorcarbonate mineralisation indicates initially relatively uniform bastnäsite and more abundant parisite, inferred to represent magmatic phases, followed by the progressive development of syntaxial intergrowth with synchysite and finally overgrowth by synchysite and röntgenite. Calcium-REE fluorcarbonates also overgrow monazite and allanite, suggesting some corrosion and REE mobility from these phases during the hydrothermal alteration stage. Because of the likely low F activity in any hydrothermal phase (Williams-Jones et al., 2012), the initial development of fluorcarbonates from earlier phases may relate to reaction with late magmatic fluids. However, subsequent alteration reactions can take place without significant addition of F. Although reactions constructed on this basis imply minimal REE mobility (Eqs. (5)–(8)), precursor normalised REE patterns again imply significant leaching of the LREE and addition of the HREE (Fig. 12F).

$$\underset{\text{Monazite}}{2REE(PO_4)} + Ca^{2+} + 3CO_3^{2-} + 2F^- = \underset{\text{Parisite}}{Ca(REE)_2(CO_3)_3F_2} + 2PO_4^{3-} \quad (5)$$

$$\underset{\text{Basnäsite}}{2REE(CO_3)F} + Ca^{2+} + CO_3^{2-} = \underset{\text{Parisite}}{Ca(REE)_2(CO_3)_3F_2} \quad (6)$$

$$\underset{\text{Parisite}}{Ca(REE)_2(CO_3)_3F_2} + Ca^{2+} + CO_3^{2-} = \underset{\text{Synchysite}}{2CaREE(CO_3)_2F} \quad (7)$$

$$\underset{\text{Parisite}}{3Ca(REE)_2(CO_3)_3F_2} + Ca^{2+} + CO_3^{2-} = \underset{\text{Röntgenite}}{2Ca_2(REE)_3(CO_3)_5F_3} \quad (8)$$

Equations for the replacement of monazite and allanite by parisite cannot be developed on the basis of an immobile crystallographic framework. However, consideration of the mineral analyses again suggests relative losses in LREE and gains in HREE from reactants to products.

Uranium and thorium have been compared as products vs precursors in Fig. 12 because both these elements may be concentrated in REE phases, and are a significant issue in the assessment of an REE resource. Thorium is typically immobile in all the reactions examined here, consistent with its low solubility in aqueous fluids (Bailey and Ragnarsdottir, 1994). Uranium shows variable behaviour throughout the alteration sequence. In the progressive alteration of aeschynite to pyrochlore U is relative immobile until the alteration of uranopyrochlore to pyrochlore, at which point it is still potentially conserved at the 10 s of micron scale, nucleating as uraninite in altered areas as small (1–50 μm) inclusions in pyrochlore. These inclusions are associated with microporosity, consistent with a dissolution-reprecipitation mechanism for niobate alteration. During the main alteration sequence the most notable change in U is in the overgrowth and replacement of the fluorcarbonates. The association of the hydrothermal stage with the formation of barite and celestine, and the presence of sulphate-rich brines within fluid inclusions, suggests that the later hydrothermal fluids where relatively oxidising, consistent with the mobilisation of U as uranyl complexes (Ragnarsdottir and Charlet, 2000).

### 5.3. Origins of HREE enrichment at Huanglongpu

The overall HREE enrichment of the Huanglongpu carbonatites has been previously related to a recycled ocean crust component in the lithospheric mantle indicated by Nd-Sr radioisotope studies and

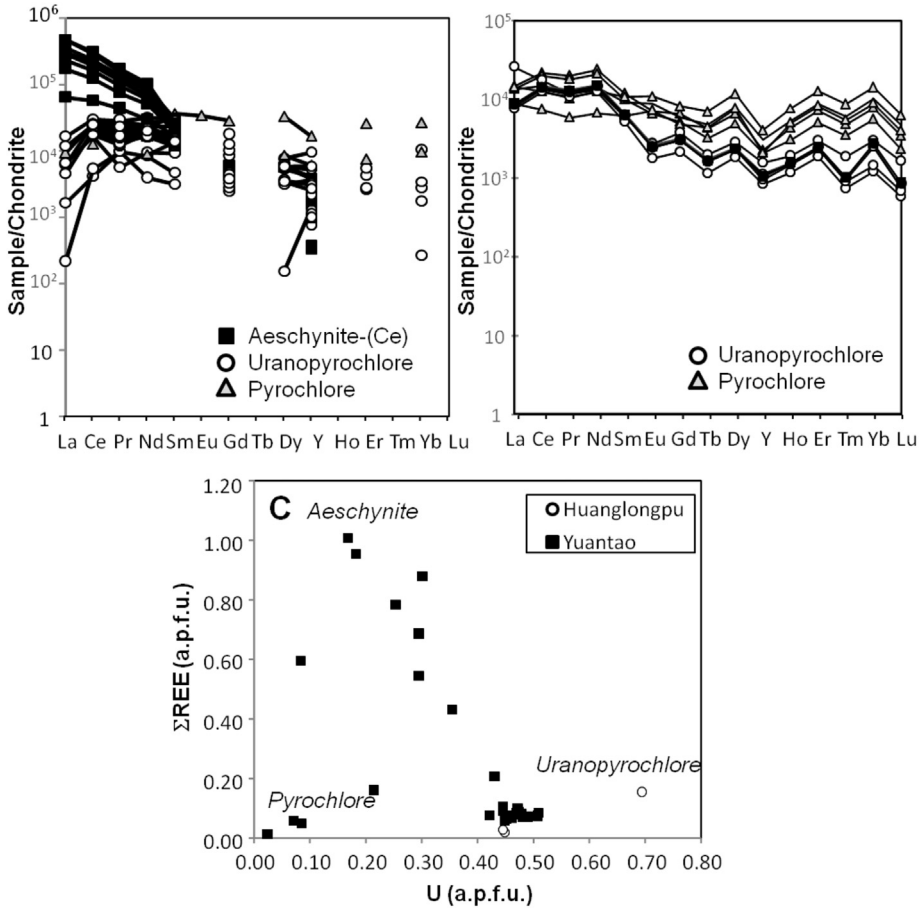


**Fig. 10.** (A) Chondrite normalised REE contents of aeschynite, uranopyrochlore and pyrochlore from EMPA. (B) Chondrite normalised REE contents of pyrochlore and uraninite from LA-ICPMS analyses. (C) Correlation of U and REE contents of aechynite and pyrochlore.

Mg stable isotope analyses of calcite (Table 8; Xu et al., 2010, 2011; Song et al., 2016), accounting for the district scale enrichment in Mo, accompanied by small degrees of melting from a garnet-poor source (Xu et al., 2007). This primary source control has been proposed to be enhanced by fractional crystallisation of calcite, with the dykes at the current level of exposure representing relatively HREE-enriched carbonate left as residuum on the walls of flowing carbonatite dykes from an initially more LREE-enriched melt (Xu et al., 2007). Both stable (O, C and S: Huang et al., 1984; Xu et al., 2010; Song et al., 2015) and radioisotope data (Xu et al., 2007, 2011), indicate that components within mineralisation originate with a primary carbonatite magma with only minor input from external fluids. The shift from carbonate dominated crystallisation to quartz and then sulphides and sulphates records the magmatic to hydrothermal transition, with variation in redox conditions during the hydrothermal stage (Huang et al., 1984), driven by either mixing with a minor external fluid component, interaction with relatively oxidised wall rocks, or phase separation. The chemical development of the mineral paragenesis during this process clearly contributed to the HREE enrichment of the final dyke rocks.

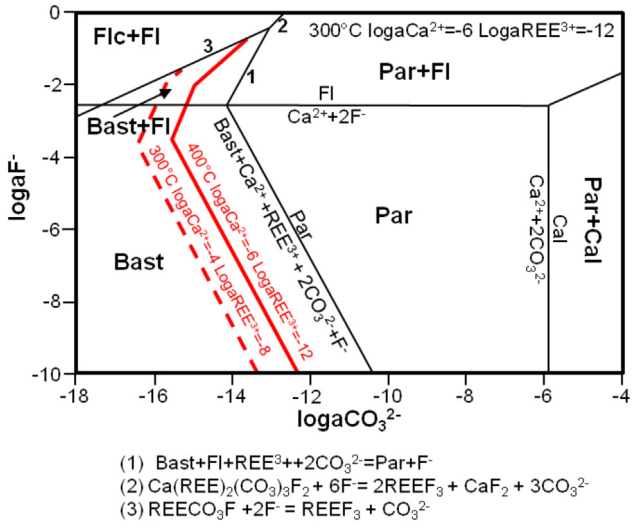


**Fig. 11.** Activity diagram for the system $REE_2O_3$-$CaF_2$-$CaCO_3$. Black lines show phase boundaries at 300 °C, $logaCa^{2+} = -6$, $logaREE^{3+} = -12$. Solid red lines show phase boundaries for the relative stability of bastnäsite and parisite at 400 °C and the same fluid composition. Dashed red lines show phase boundaries for the relative stability of bastnäsite and parisite at 300 °C, $logaCa^{2+} = -4$, $logaREE^{3+} = -8$. Adapted from Gysi and Williams-Jones (2015). (For interpretation of the references to colour in this figure legend, the reader is referred to the web version of this article.)

The trends developed in the REE patterns at Huanglongpu can be explained by consideration of experimental data on solubility of REE minerals and aqueous complex stability for REE species. Solubility products for fluorides and phosphates are higher for Y and HREE than for LREE (Migdisov et al., 2009; Tropper et al., 2011; Fig. 13A). The preferentially solubility of the HREE end-members in low ligand strength fluids cannot therefore result in passive enrichment in the HREE. However, ligand concentrations can significantly modify this behaviour. Experimental data at 1GPa and 800 °C) have shown Ce-monazite becomes more soluble than Y-xenotime at high $X_{NaCl}$ and low $X_{NaF}$ (where X is mole fraction; Tropper et al., 2011, 2012). Determinations of $LnCl^{2+}$ aqueous complex ion stability constants ($Log\beta_1$) show that chloride preferentially forms complex ions with the LREE, and hence would promote LREE-mineral solubility at high concentrations (Fig. 13B). Low solubility

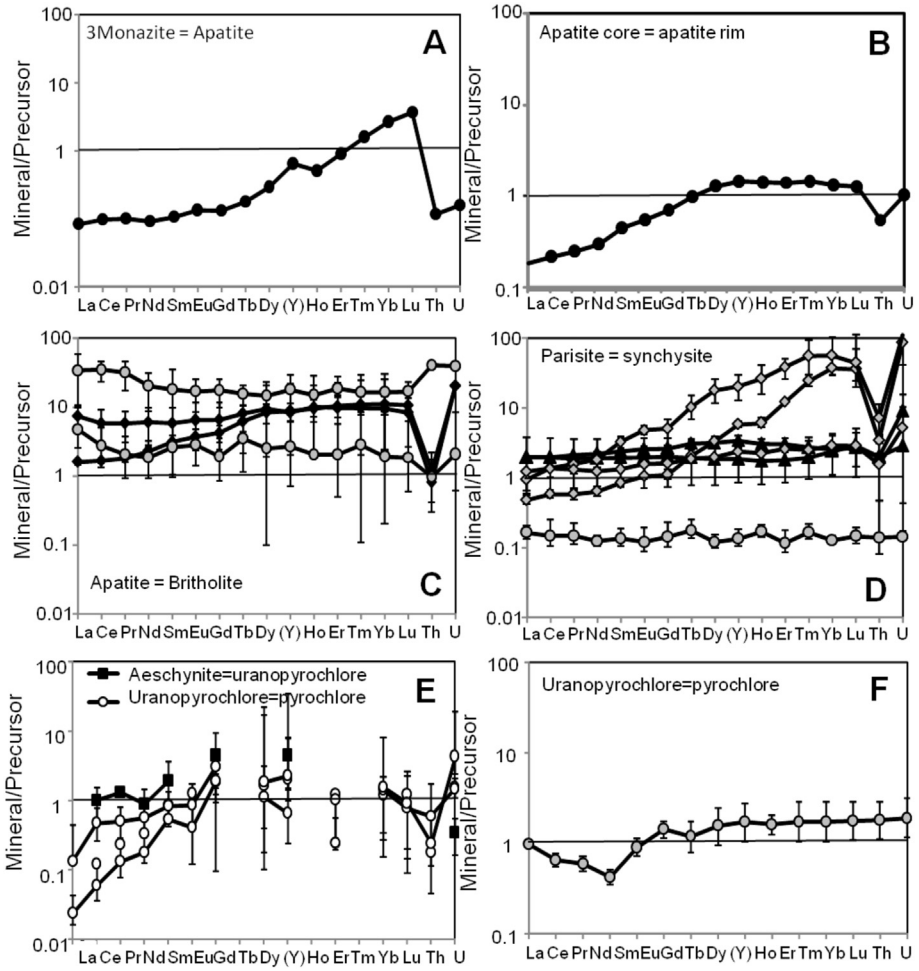


**Fig. 12.** Product to precursor normalised REE plots in relation to reaction textures, taking into account reaction stoichiometry assuming immobile framework ions. Error bars are based on 2σ of the mean of analyses on individual reaction textures where $N = 2$ or more. (a) Reaction of monazite to apatite. (b) Apatite core normalised to leached apatite rim. (c) Reaction of apatite to britholite. (d) Reaction of parasite to synchysite. (e) Reaction of aeschynite to pyrochlore, and pyrochlore to uranopyrochlore (EPMA). (f) Reaction of Pyrochlore to urnaopyrchlore (LA-ICPMS).

constants for fluocerite and fluorcarbonate minerals (Williams-Jones et al., 2012) mean high F activities are unlikely to have a major role. A process of preferential LREE mineral solubility enhanced by chloride complex formation is likely to have resulted in the LREE depletion of monazite on the formation of apatite, the subsequent depletion of apatite rims, and the progressive leaching of the REE during alteration from aeschynite to pyrochlore. It cannot, however, account for the significant addition of the HREE inferred in the alteration of apatite to britholite, and the alteration of parisite and bastnäsite to synchysite and röntgentite.

**Table 8**
Summary of previous radio- and stable isotopic data from Huanglongpu. Data are consistent with an enriched mantle source, with a possible subducted carbonate component. Narrow ranges for stable isotope data suggest limited mixing of fluid sources, and are consistent with a mantle-derived carbonatite origin for fluids and solution components including S.

| Reference | Isotope System | Min | Max | | Estimated fluid composition |
|---|---|---|---|---|---|
| Song et al. (2016) | $\delta^{25}$Mg (‰) | −0.68 | −0.56 | $n = 9$ | |
| | $\delta^{26}$Mg (‰) | −1.28 | −1.07 | n = 9 | |
| | $\delta^{34}$S sulphides (‰) | −10.5 | −6.5 | $n = 18$ | ~1‰ |
| | $\delta^{34}$S Barite (‰) | 4.6 | 5.1 | $n = 6$ | |
| Xu et al. (2011) | $^{87}Sr/^{86}Sr_i$ | 0.705 | 0.706 | $n = 10$ | |
| | $\varepsilon_{Nd(t, CHUR)}$ | −10.1 | −4.3 | n = 10 | |
| | $^{207}Pb/^{206}Pb_i$ | 0.883 | 0.887 | n = 10 | |
| | $^{208}Pb/^{206}Pb_i$ | 2.146 | 2.159 | n = 10 | |
| Song et al. (2015) | $\delta^{18}$O quartz | 8.1 | 10.2 | $n = 5$ | |
| Xu et al. (2010) | $\delta^{18}$O calcite | 7.2 | 9.2 | $n = 8$ | |
| | $\delta^{13}$C calcite | −6.9 | −6.5 | n = 8 | |
| Huang et al. (1984) | $\delta^{34}$S sulphides | −14.7 | −4 | $n = 25$ | ~1‰ |
| | $\delta^{34}$S Barite | 4.7 | 7.9 | n = 8 | |
| | $\delta^{18}$O calcite | 8.5 | 9.5 | n = 8 | |
| | $\delta^{13}$C calcite | −7 | −6.6 | n = 8 | |

Late enrichment in the HREE is observable in calcite, and indicates that the Huanglongpu system evolved to HREE-rich conditions, presumably because of higher initial HREE contents in the original magma (Xu et al., 2007). For hydrothermal fluids at this later stage to have developed high HREE contents requires either direct reaction with HREE-rich calcite, or a mechanism allowing fluids to either partition HREE preferentially from late stage melts. Very few commonly occurring ligands are HREE-selective, although the contrast in formation constants between the LREE and HREE declines at lower T. However, theoretical extrapolation of stability constants from low T data (Haas et al., 1995; Wood, 1990) and experimental data (Migdisov and Williams-Jones, 2008) all indicate $SO_4^{2-}$ is a possible ligand with minimal difference in stability between LREE and HREE (Fig. 13B). Carbonate is also a potentially less LREE selective ligand at hydrothermal temperatures (Haas et al., 1995). Fluid inclusion data from quartz cores to the carbonatite dykes (Cangelosi, 2016; Song et al., 2016) indicate hydrothermal fluids in the Huanglongpu district were saturated with respect to sulphate minerals, and arcanite ($K_2SO_4$), anhydrite ($CaSO_4$), glauberite ($Na_2Ca(SO_4)_2$), and gorgeyite ($K_2Ca_5(SO_4)_6{\cdot}H_2O$) have all

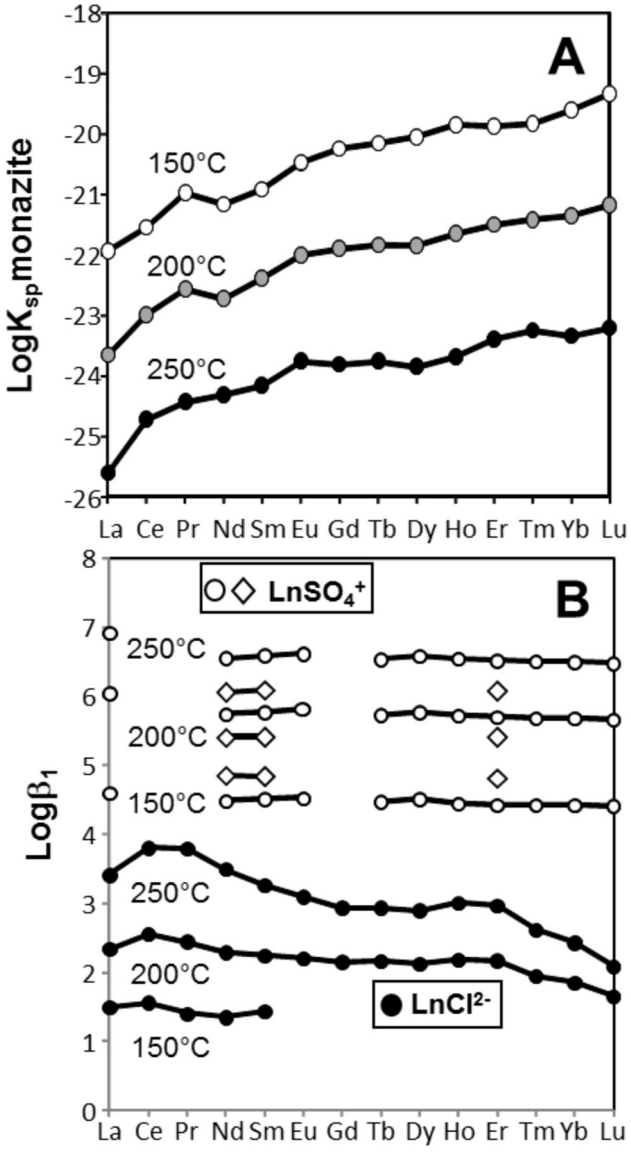


**Fig. 13.** (A) Solubility products ($K_{sp}$) for monazite from 150 to 250 °C from Migdisov et al. (2009). (B) Experimentally determined first association constants for Ln-Cl (Migdisov et al., 2009) and Ln-$SO_4$ (Migdisov and Williams-Jones, 2008) aqueous complexes from 100 to 250 °C and 10 MPa. First association constants for REE-$SO_4$ complexes calculated from the data of Haas et al. (1995) are shown for comparison (open circles).

been identified as either daughter or heterogeneously trapped phases in fluid inclusions (Cangelosi, 2016). Migdisov et al. (2016) demonstrated that sulphate complexes of the form $REE(SO_4)_2^-$ can predominate in fluoride-containing, Cl-dominated brines at intermediate pH (~3–8), from 200 to 400 °C in the presence of cerianite. These conditions are entirely consistent with the example studied here. Dissolution of calcite as pH falls with decreasing T, in the presence of sulphate and carbonate ligands has the potential to release HREE from calcite resulting in the formation of late HREE enriched minerals.

### 5.4. Wider implications

Sulphate is a component in many carbonatite melts (e.g. Doroshkevich et al., 2010; Xie et al., 2015), and sulphate melt generated by immiscibility in the late stages of magmatic crystallisation has been identified in numerous melt inclusion studies (e.g. Andreeva et al., 1998; Panina, 2005; Panina and Motorina, 2008; Panina and Stoppa, 2009). Equally, sulphate-rich fluids within carbonatite-related hydrothermal systems are widespread, with barite and celestine as common accessories in carbonatite systems (e.g. Nikiforov et al., 2014; Trofanenko et al., 2016; Xie et al., 2015). The key factor for the genesis of sulphide- or sulphate-bearing carbonatite systems is the redox state of the melt or fluid. In the magmatic stage oxidised carbonatite melts have been proposed to be generated by oxidised mantle source regions (Foley, 2011) and magma mingling (Moore et al., 2009), whilst in hydrothermal systems the redox state of the fluid is controlled by interaction with the host-rocks, mineral deposition and phase separation (Robb, 2005). There is widespread evidence for sulphate complexation of the REE from mesothermal to epithermal systems (e.g. Inguaggiato et al., 2015; Lewis et al., 1998). The inference that sulphate-rich brines are responsible for the late HREE-enrichment of the REE mineral assemblage means that REE-rich carbonatites with strong evidence for sulphate-bearing magmas and late stage sulphate alteration may be prospective targets for relative HREE-enrichment, although initial HREE-enrichment in the mantle source is still a necessity for significant HREE mineralisation. Previous research and mineral exploration has identified HREE-enriched zones in a number of potentially economically mineralised carbonatites, reviewed briefly in the introduction. In most of these HREE-enrichment is related to sub-solidus hydrothermal processes associated with barite and celestine deposition (Broom-Fendley et al., 2017; Moore et al., 2017; Ngwenya, 1993). At Lofdal the main HREE enrichment was inferred to be hydrothermal, associated with carbonate matrices to breccias (Bodeving et al., 2017) with less evidence for high sulphare activities. Thus carbonatite HREE-mineralisation is very commonly hydrothermal in origin, and frequently associated with sulphate-rich fluids. Both $SO_4^{2-}$ and $CO_3^{2-}$ are potentially less LREE-selective ligands which may contribute to HREE leaching and transport during secondary processes, and may be effectiviely destabilised by processes such as boiling, aqueous-carbonic immiscibility and water-rock interaction, whilst $Cl^-$ acts to retain LREE in the fluid. Although the HREE-enrichment at Huanglongpu is a function of both magma source regions and hydrothermal enrichment, the processes identified here clearly have the potential to operate in many carbonatite-related hydrothermal systems.

## 6. Conclusions

The carbonatites of the Huanglongpu district, Qinling mountains, China, are REE-mineralised, and HREE-enriched compared to typical carbonatites and carbonatite-related REE deposits. The dykes and veins evolved from early calcite dominated crystallisation to multiple stages of late magmatic and hydrothermal activity generating multiple generations of carbonate, K-feldspar and quartz-rich cores to the dykes. Textural and geochemical data show that the REE and niobate mineral assemblage evolved via fractional crystallisation from an early magmatic stage dominated by monazite-(Ce), parisite-(Ce) and aeschynite-(Ce), to more REE depleted conditions resulting in the overgrowth and replacement of monazite by apatite, and the alteration of aeschynite to uranopyrochlore. Subsequent alteration reactions record the shift to silica-rich hydrothermal conditions at temperatures from 300 to 200 °C, 0.5-1 kbar, and involving aqueous-carbonic brines, resulting in the alteration of apatite to britholite-(Ce) and the crystallisation of allanite-(Ce). Cooling of the hydrothermal system to >265 °C moved REE mineralisation to fluorcarbonate mineral dominated, and reaction with host carbonatite resulted in raised $a_{Ca^{2+}}$ and $a_{CO_3^{2-}}$, causing alteration of early fluorcarbonates to synchysite and röntgenite. At every stage of alteration hydrothermal fluids leached the LREE relative to the HREE. Solubility products for LREE minerals are typically lower than for HREE except in the presence of strong ligands, in this case probably $Cl^-$, $CO_3^{2-}$ and $SO_4^{2-}$. For some replacement reactions the increase in the HREE concentration cannot be accounted for by passive enrichment without significant volume loss, and so there must have been a metasomatic flux of the HREE. The host calcite is the most likely source of HREE as the overall carbonatite system is anomalously HREE-enriched compared to typical systems. The sulphate-rich nature

of metasomatic brines provides a mechanism via which this may occur, as sulphate complexes show no major difference between LREE and HREE complex ion stability. There is no evidence for a major role for fluoride in this process, except as a depositional ligand in the precipitation of fluorcarbonate minerals. Globally sulphate-rich carbonatites may therefore offer significant potential for more HREE enriched carbonatite-related resources.

Supplementary data to this article can be found online at https://doi.org/10.1016/j.lithos.2018.02.027.

## Acknowledgements

We would like to thank Andrew Flint and Mike Helias for additional help with SEM imaging at the University of Brighton. The manuscript was improved by comments from Nelson Eby and two anonymous referees.

## Funding

This work was supported by the NERC SOS:RARE project (NE/M011267/1), the EU H2020 (grant agreement no. 689909), grant project (HiTech AlkCarb) and project CEITEC 2020 (LQ1601).

## References

Andreeva, I.A., Naumov, V.B., Kovalenko, V.I., Kononkova, N.N., 1998. Fluoride-sulfate and chloride-sulfate salt melts of the carbonatite-bearing complex Mushugai-Khuduk, southern Mongolia. Petrology 6, 284–292.

Bailey, E.H., Ragnarsdottir, V., 1994. Uranium and thorium solubilities in subduction zone fluids. Earth and Planetary Science Letters 124, 119–129.

Bodeving, S., Williams-Jones, A.E., Swinden, S., 2017. Carbonate–silicate melt immiscibility, REE mineralising fluids, and the evolution of the Lofdal intrusive suite, Namibia. Lithos 268–271, 383–398.

Bowers, T.S., Helgeson, H.C., 1983. Calculation of the thermodynamic and geochemical consequences of non-ideal mixing in the system $H_2O$-$CO_2$-NaCl on phase relations in geologic systems: equation of state for $H_2O$-$CO_2$-NaCl fluids at high pressures and temperatures. Geochimica et Cosmochimica Acta 47, 1247–1275.

Broom-Fendley, S., Styles, M.T., Appleton, J.D., Gunn, G., Wall, F., 2016. Evidence for dissolution-reprecipitation of apatite and preferential LREE mobility in carbonatite-derived late-stage hydrothermal processes. American Mineralogist 101, 596–611.

Broom-Fendley, S., Brady, A.E., Wall, F., Gunn, G., Dawes, W., 2017. REE minerals at the Songwe Hill carbonatite, Malawi: HREE-enrichment in late-stage apatite. Ore Geology Reviews 81, 23–41.

Cangelosi, D., 2016. The Heavy Rare Earth Element Enrichment of the Huanglongpu deposit, China. (MRes Thesis). Leeds Univ., UK.

Chakhmouradian, A.R., 2006. High-field-strength elements in carbonatitic rocks: geochemistry, crystal chemistry and significance for constraining the sources of carbonatites. Chemical Geology 235, 138–160.

Chakhmouradian, A., Wall, F., 2012. Rare earth elements: minerals, mines, magnets (and more). Elements 8, 333–340.

Doroshkevich, A.G., Ripp, G.S., Moore, K.R., 2010. Genesis of the Khaluta alkaline-basic Ba-Sr carbonatite complex (West Transbaikala, Russia). Mineralogy and Petrology 98, 245–268.

Ecrit, T.S., 2005. Identification and alteration trends of granitic-pegmatite-hosted (Y, REE, U, Th)-(Nb, Ta, Ti) oxide minerals: a statistical approach. Canadian Mineralogist 43, 1291–1303.

Foley, S.F., 2011. A reappraisal of redox melting in the Earth's mantle as a function of tectonic setting and time. Journal of Petrology 52, 1363–1391.

Gysi, A.P., Williams-Jones, A.E., 2015. The thermodynamic properties of bastnäsite-(Ce) and parisite-(Ce). Chemical Geology 392, 87–101.

Haas, J.R., Shock, E.L., Sassani, D.C., 1995. Rare earth elements in hydrothermal systems: estimates of standard partial molal thermodynamic properties of aqueous complexes of the rare earth elements at high pressures and temperatures. Geochimica et Cosmochimica Acta 59, 4329–4350.

Henderson, P., 1984. Rare earth element geochemistry. Developments in Geochemistry. 2. Elsevier.

Hornig-Kjarsgaard, I., 1998. Rare earth elements in Sövitic carbonatites and their mineral phases. Journal of Petrology 39, 2105–2121.

Huang, D.H., Wang, Y., Nie, F., Jiang, X., 1984. Isotopic composition of sulphur, carbon and oxygen and source material of the Huanglongpu carbonatite vein-type of molybdenum (lead) deposits. Acta Geologica Sinica 63, 252–264 (in Chinese with English abstract).

Huang, D.H., Wu, C.Y., Du, A.D., He, H.L., 1994. Re–Os isotope age of molybdenum deposits in east Qinling and their significance. Mineral Deposits 13, 221–230 (in Chinese with English abstract).

Inguaggiato, C., Censi, P., Zuddas, P., Londono, J.M., Chacon, Z., Alzate, D., Brusca, L., D'Alessandro, W., 2015. Geochemistry of REE, Zr and Hf in a wide range of pH and water composition: the Nevado del Ruiz volcano-hydrothermal system (Colombia). Chemical Geology 417, 125–133.

Kynicky, J., Smith, M.P., Xu, C., 2012. Diversity of rare earth deposits: the key example of China. Elements 8, 361–367.

Le Bas, M.J., 1987. Nephelinites and Carbonatites. In: Fitton, J.G., Upton, B.G. (Eds.), Proceedings of Rare Earths'04 MS. International Journal of Mass Spectrometry vol. 253, pp. 87–97.

Lewis, A.J., Komninou, A., Yardley, B.W.D., Palmer, M.R., 1998. Rare earth element speciation in geothermal fluids from Yellowstone National Park, Wyoming, USA. Geochimica et Cosmochimica Acta 62, 657–663.

Lumpkin, G.R., Ewing, R.C., 1992. Geochemical alteration of pyrochlore group minerals: microlite subgroup. American Mineralogist 77, 179–188.

Lumpkin, G.R., Ewing, R.C., 1995. Geochemical alteration of pyrochlore group minerals: Pyrochlore subgroup. American Mineralogist 80, 732–743.

Lumpkin, G.R., Ewing, R.C., 1996. Geochemical alteration of pyrochlore group minerals: Betafite subgroup. American Mineralogist 81, 1237–1248.

Mao, J.W., Xie, G.Q., Bierlein, F., Qu, W.J., Du, A.D., Ye, H.S., Pirajno, F., Li, H.M., Guo, B.J., Li, Y.F., Yang, Z.Q., 2008. Tectonic implications from Re-Os dating of Mesozoic molybdenum deposits in the East Qinling-Dabie orogenicbelt. Geochimica et Cosmochimica Acta 72, 4607–4626.

Meng, Q.R., Zhang, G.W., 2000. Geologic framework and tectonic evolution of the Qinling orogen, Central China. Tectonophysics 323, 183–196.

Migdisov, A.A., Williams-Jones, A.E., 2008. A spectrophotometric study of Nd(III), Sm(III) and Er(III) complexation in sulfate-bearing solutions at elevated temperatures. Geochimica et Cosmochimica Acta 72, 5291–5303.

Migdisov, A.A., Williams-Jones, A.E., Wagner, T., 2009. An experimental study of the solubility and speciation of the rare earth elements (III) in fluoride- and chloride-bearing aqueous solutions at temperatures up to 300°C. Geochimica et Cosmochimica Acta 73, 7087–7109.

Migdisov, A., Williams-Jones, A.E., Brugger, J., Caporuscio, F.A., 2016. Hydrothermal transport, deposition, and fractionation of the REE: experimental data and thermodynamic calculations. Chemical Geology 439, 13–42.

Mitchell, R., 2005. Carbonatites and carbonatites and carbonatites. Canadian Mineralogist 43, 2049–2068.

Mitchell, R., 2015. Primary and secondary niobium mineral deposits associated with carbonatites. Ore Geology Reviews 64, 626–641.

Moore, K.R., Wall, F., Divaev, F.K., Savatenkov, V.M., 2009. Mingling of carbonate and silicate magmas under turbulent flow conditions: evidence from rock textures and mineral chemistry in subvolcanic carbonatite dykes, Chagatai, Uzbekistan. Lithos 110, 65–82.

Moore, M., Chakhmouradian, A., Mariano, A.N., Sidhu, R., 2017. Evolution of rare-earth mineralization in the bear lodge carbonatite, Wyoming: mineralogical and isotopic evidence. Ore Geology Reviews 64, 499–521.

Ngwenya, B., 1993. Hydrothermal rare earth mineralisation in carbonatites of the Tundulu complex, Malawi: processes at the fluid/rock interface. Geochimica et Cosmochimica Acta 58, 2061–2072.

Nikiforov, A.V., Ozturk, H., Altuncu, S., Lebedev, V.A., 2014. Kizilcaoren ore-bearing complex with carbonatites (northwestern Anatolia, Turkey): formation time and mineralogy of rocks. Geology of Ore Deposits 56, 35–60.

Panina, L.I., 2005. Multiphase carbonate-salt immiscibility in carbonatite melts: data on melt inclusions from the Krestovskiy massif minerals (polar Siberia). Contributions to Mineralogy and Petrology 150, 19–36.

Panina, L.I., Motorina, I.V., 2008. Liquid immiscibility in deep-seated magmas and the generation of carbonatite melts. Geochemistry International 46, 448–464.

Panina, L.I., Stoppa, F., 2009. Silicate-carbonate-salt liquid immiscibility and origin of the sodalite-haüyne rocks: study of melt inclusions in olivine foidite from vulture volcano, S. Italy. Central European Journal of Geosciences 1, 377–392.

Pouchou, J.L., Pichoir, F., 1984. A New Model for Quantitative Analyses. I. Application to the Analysis of Homogeneous Samples. 3. La Recherche Aérospatiale, pp. 13–38.

Putnis, A., 2002. Mineral replacement reactions: from macroscopic observations to microscopic mechanisms. Mineralogical Magazine 66, 689–708.

Ragnarsdottir, K.V., Charlet, L., 2000. Uranium behaviour in natural environments. In: Cotter-Howells, J., Batchelder, M., Valsami-Jones, E. (Eds.), Environmental Mineralogy. Mineralogical Society of Great Britain and Ireland, London, pp. 333–377.

Ratschbacher, L., Hacker, B.R., Calvert, A., Webb, L.E., Grimmer, J.C., McWilliams, M.O., Ireland, T., Dong, S., Hu, J., 2003. Tectonics of the Qinling (Central China): tectonostratigraphy, geochronology, and deformation history. Tectonophysics 366, 1–53.

Robb, L., 2005. Introduction to Ore Forming Processes. Blackwell Science, Oxford (373 pp.).

Smith, M.P., Henderson, P., Campbell, L.S., 2000. Fractionation of the REE during hydrothermal processes: constraints from the Bayan obo Fe–REE–Nb deposit, Inner Mongolia, China. Geochimica et Cosmochimica Acta 64, 3141–3160.

Song, W., Xu, C., Qi, L., Zhou, L., Wang, L., Kynicky, J., 2015. Genesis of Si-rich carbonatites in Huanglongpu Mo deposit, lesser Qinling orogen, China and significance for Mo mineralization. Ore Geology Reviews 64, 756–765.

Song, W., Xu, C., Smith, M.P., Kynicky, J., Huang, K., Wei, C., Li, Zhou, Shu, Q., 2016. Origin of Unusual HREE-Mo-rich Carbonatites in the Qinling Orogen, China. Scientific Reports 6:37377. https://doi.org/10.1038/srep37377.

Stein, H.J., Markey, R.J., Morgan, M.J., Du, A., Sun, Y., 1997. Highly precise and accurate Re–Os ages for molybdenite from the east Qinling–Dabie molybdenum belt, Shaanxi province, China. Economic Geology 92, 827–835.

Sun, S.-S., McDonough, W.F., 1989. Chemical and isotopic systematics of oceanic basalts: implications for mantle composition and processes. In: Saunders, A.D., Norry, M.J. (Eds.), Magmatism in Ocean Basins. Geol. Soc. Spec. Publ., London, pp. 313–345.

Swinden, S., Hall, M., 2012. NI 43-101 Technical Report and Mineral Resource Estimate for the Songwe Hill Rare Earth Element (REE) Project, Phalombe District, Republic of Malawi (Report prepared for Mkango Resources by MSA group. 168 pp.).

Trofanenko, J., Williams-Jones, A.E., Simandl, G.J., Migdisov, A.A., 2016. The nature and origin of the REE mineralization in the Wicheeda carbonatite, British Columbia, Canada. Economic Geology 111, 199–223.

Tropper, P., Manning, C.E., Harlov, D.E., 2011. Solubility of $CePO_4$ monazite and $YPO_4$ xenotime in $H_2O$ and $H_2O$–NaCl at 800 °C and 1 GPa: implications for REE and Y transport during high-grade metamorphism. Chemical Geology 282, 58–66.

Tropper, P., Manning, C.E., Harlov, D.E., 2012. Experimental determination of $CePO_4$ and $YPO_4$ solubilities in $H_2O$–NaF at 800 °C and 1 GPa: implications for rare earth element transport in high-grade metamorphic fluids. Geofluids 13, 372–380.

Wall, F., Niku-Paavola, V.N., Storey, C., Muller, A., Jeffries, T., 2008. Xenotime-(Y) from carbonatite dykes at Lofdal, Namibia: unusually low LREE:HREE ratio in carbonatite, and the first dating of xenotime overgrowths on zircon. Canadian Mineralogist 46, 861–877.

Williams, C.T., 1996. Analysis of rare earth minerals. In: Jones, A.P., Wall, F., Williams, C.T. (Eds.), Rare Earth Minerals: Chemistry, Origin and Ore Deposits. Chapman and Hall, pp. 327–348.

Williams-Jones, A.E., Wood, S.A., 1992. A preliminary petrogenetic grid for REE fluorocarbonates and associated minerals. Geochimica et Cosmochimica Acta 56, 725–738.

Williams-Jones, A.E, Migdisov, A.A., Samson, I.M., 2012. Hydrothermal mobilization of the rare earth elements – a tale of 'ceria' and 'yttria'. Elements 8, 355–360.

Williams-Jones, A.E., Migdisov, A.A., Samson, I.M., 2013. Hydrothermal mobilisation of the rare earth elements - a tale of "ceria" and "Yttria". Elements 8, 355–360.

Wood, S.A., 1990. The aqueous geochemistry of the rare earth elements and yttrium. Part I. Review of available low temperature data for inorganic complexes and the inorganic REE speciation of natural waters. Chemical Geology 82, 159–186.

Xie, Y.L., Li, Y.X., Hou, Z.Q., Cooke, D.R., Danyushevsky, L., Dominy, S.C., Yin, S.P., 2015. A model for carbonatite hosted REE mineralisation - the Mianning-Dechang REE belt, western Sichuan Province, China. Ore Geology Reviews 70, 595–612.

Xu, C., Campbell, I.H., Allen, C.M., Huang, Z.L., Qi, L., Zhang, H., Zhang, G.S., 2007. Flat rare earth element patterns as an indicator of cumulate processes in the lesser Qinling carbonatites, China. Lithos 95, 267–278.

Xu, C., Kynicky, J., Chakhmouradian, A., Qi, L., Song, W., 2010. A unique Mo deposit associated with carbonatites in the Qinling orogenic belt, central China. Lithos 118, 50–60.

Xu, C., Taylor, R.N., Kynicky, J., Chakhmouradian, A., Song, W., Wang, L., 2011. The origin of enriched mantle beneath North China block: evidence from young carbonatites. Lithos 127, 1–9.

Xu, C., Chakhmouradian, A., Taylor, R.N., Kynicky, J., Li, W., Song, W., Fletcher, I.R., 2014. Origin of carbonatites in the south Qinling orogen: implications for crustal recycling and timing of collision between the south and North China blocks. Geochimica et Cosmochimica Acta 143, 189–206.

Xue, F., Lerch, M.F., Kroner, A., Reischmann, T., 1996. Tectonic evolution of the east Qinling Mountains, China, in the Palaeozoic: a review and new tectonic model. Tectonophysics 253, 271–284.

Zaitsev, A.N., Wall, F., Le Bas, M.J., 1998. REE-Sr-Ba minerals from the Khibina carbonatites, Kola peninsula, Russia: their mineralogy, paragensis and evolution. Mineralogical Magazine 62, 225–250.

Zaitsev, A.N., Demény, A., Sinder, S., Wall, F., 2002. Burbankite group minerals and their alteration in rare earth carbonatites – source of elements and fluids (evidence from C-O and Sr-Nd isotopic data). Lithos 62, 15–33.

Zhao, H., Mao, J., Ye, H., Xie, G., Yang, Z., 2010. Geochronology and geochemistry of the alkaline granite porphyry and diabase dikes in Huanglongpu area of Shaanxi Province: petrogenesis and implications for tectonic environment. Geology in China 37 (1), 12–27 (in Chinese with English abstract).